Geometry and Anchoring Effects on Elliptic Cylinder Domains of Nematic Phases

by

Pouya Khayyatzadeh

A thesis
presented to the University of Waterloo
in fulfillment of the
thesis requirement for the degree of
Master of Applied Science
in
Chemical Engineering

Waterloo, Ontario, Canada, 2014

I hereby declare that I am the sole author of this thesis. This is a true copy of the thesis, including any required final revisions, as accepted by my examiners.

I understand that my thesis may be made electronically available to the public.

Abstract

Compounds which exhibit liquid crystal phases have been widely used in display technology. The majority of display applications utilize the nematic liquid crystal phase, which is a liquid-like phase which has partial orientational order at the molecular level. The nematic phase exhibits birifringence which can be manipulated through the application of an external field. Subsequently, all liquid crystal-based display technology utilizes the application of an external field to "switch" or tune the optical properties of a nematic domain into a desired optical state. In addition to an external field, the geometry and surface interactions of the liquid crystal domain must be precisely controlled in order for the display to operate properly. Liquid crystal displays (LCDs) utilize a rectangular domain, or pixel, within which the nematic domain is exposed to surface anchoring conditions that result in a twist of the nematic alignment through the thickness of the domain.

In this work, a different type of liquid crystal domain that is elliptic is studied which is formed through "bottom-up" techniques, such as phase separation of a liquid crystal/polymer mixture to form a polymer-dispersed liquid crystal (PDLC) composite. Nematic domains within PDLCs are spheroidal, as opposed to rectangular for a pixel, and thus exhibit substantially different behaviour in the presence of an external field. The fundamental difference between spheroidal and rectangular nematic domains is that the former requires the presence of defects in nematic order while the latter does not.

The overall objective of this work is to study, for a simplified elliptic cylinder domain, the formation of the nematic domain, the resulting domain texture in the presence of an external field, and the domain texture following release of the external field. These three states are directly related to applications of PDLC films as optical functional materials, where an external (electric) field is used to manipulate the optical properties of the film. The effects of geometry (aspect ratio), surface anchoring, and external field strength are studied through a simulation-based approach using the Landau-de Gennes theory of the nematic phase.

Acknowledgements

I would like to thank my supervisor Professor Abukhdeir and all the people who made this thesis possible.

Dedication

This thesis is dedicated to my parents and Sara.

Table of Contents

List of Tables

List of Figures

Chapter 1

Introduction

1.1 Discovery of Liquid Crystals

The story of liquid crystals begins with experimental works of a pioneering chemist named Friedrich Reinitzer in 1888 [8]. He was also a botanist and conducted studies on chemicals extracted from different types of plants. While attempting to measure the molecular weight of one of these compounds, cholesterol, he encountered an unexpected property of its melting point. Reinitzer found that cholesterol exhibits two melting points – one at 145.5C and another at 178.5C. He wrote a letter to his colleague, Otto Lehmann, and told him about this anomalous behaviour of the compound.

Lehmann conducted his own experiments and confirmed the observations of Reinitzer [8]. Different intermediate phases were recognized in the melting process, which means there is no sharp transition from solid to liquid and vice versa. Examining the phase transition sequence of cholesterol under microscope with crossed polarizers resulted in observations of a solid to a blue and violet phase and then to a turbid liquid and again another blue phase and finally liquid phase. There are two contradictions in this observation:

- On one hand, getting a cloudy liquid from a solid is not possible due to the high degree of purity of the substance.
- A liquid cannot melt and form another liquid by increasing temperature since at concerned temperatures decomposition is impossible.

Further experiments were performed which involved a cooling process and under polarized light he observed that some aggregates form and grow which would eventually connect

together to form thread-like objects. Since these stripes were in contrast with the background he called them oily streaks, shown in Figure 1.1. Based on this observation and the fact that the substance is still capable of flow, Lehmann came to the conclusion that there exist some sort of order in one direction which can interact with polarized light and there is also disorder in another direction that allows the material to flow. He proposed that intermediate phases can exist between the liquid and solid states and initiated the liquid crystal field in physics.

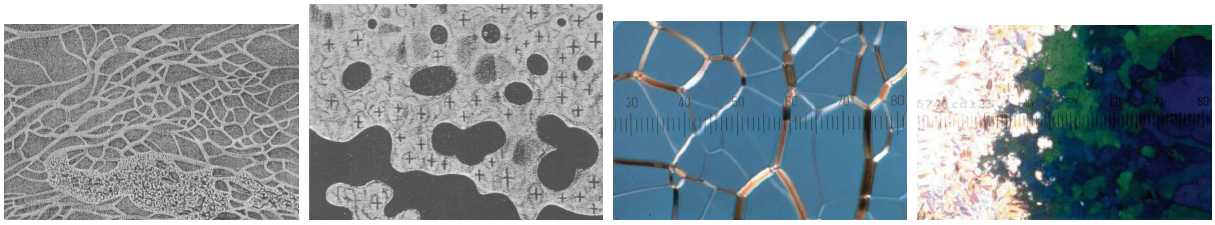

(a) (b) (c) (d)

Figure 1.1: Polarized optical microscopy images of "oily streaks." (a-b) taken from ref. [1] and (c-d) are taken from ref. [8].

1.2 Classification of LCs

As mentioned in the previous section, liquid crystals (LC) are intermediate or mesomorphic phases [3]. In a typical crystalline material molecules are located regularly on a three dimensional lattice (Figure 1.2a). On the other hand, liquids possess no order apart from an average intermolecular separation distance (Figure 1.2b). Classification of LC order falls into two major types: orientational order (Figure 1.2c) and positional (Figure 1.2d). The latter refers to the extent of arrangement of molecules centre of mass in any kind of ordered pattern. For this reason, liquids have no positional order and are considered an isotropic phase, meaning that the phase is invariant by all rotations and reflections about any point of the medium [9]. The former corresponds to the degree of alignment of non-spherical molecules along an axis. Thus in all LC phases a local preferred molecular axis is present. This leads to classification of LCs based upon the presence and type of positional order observed. With the above description in mind, we can distinguish three liquid crystal types:

Nematics. This class of liquid crystal order has no positional order and corresponds to a

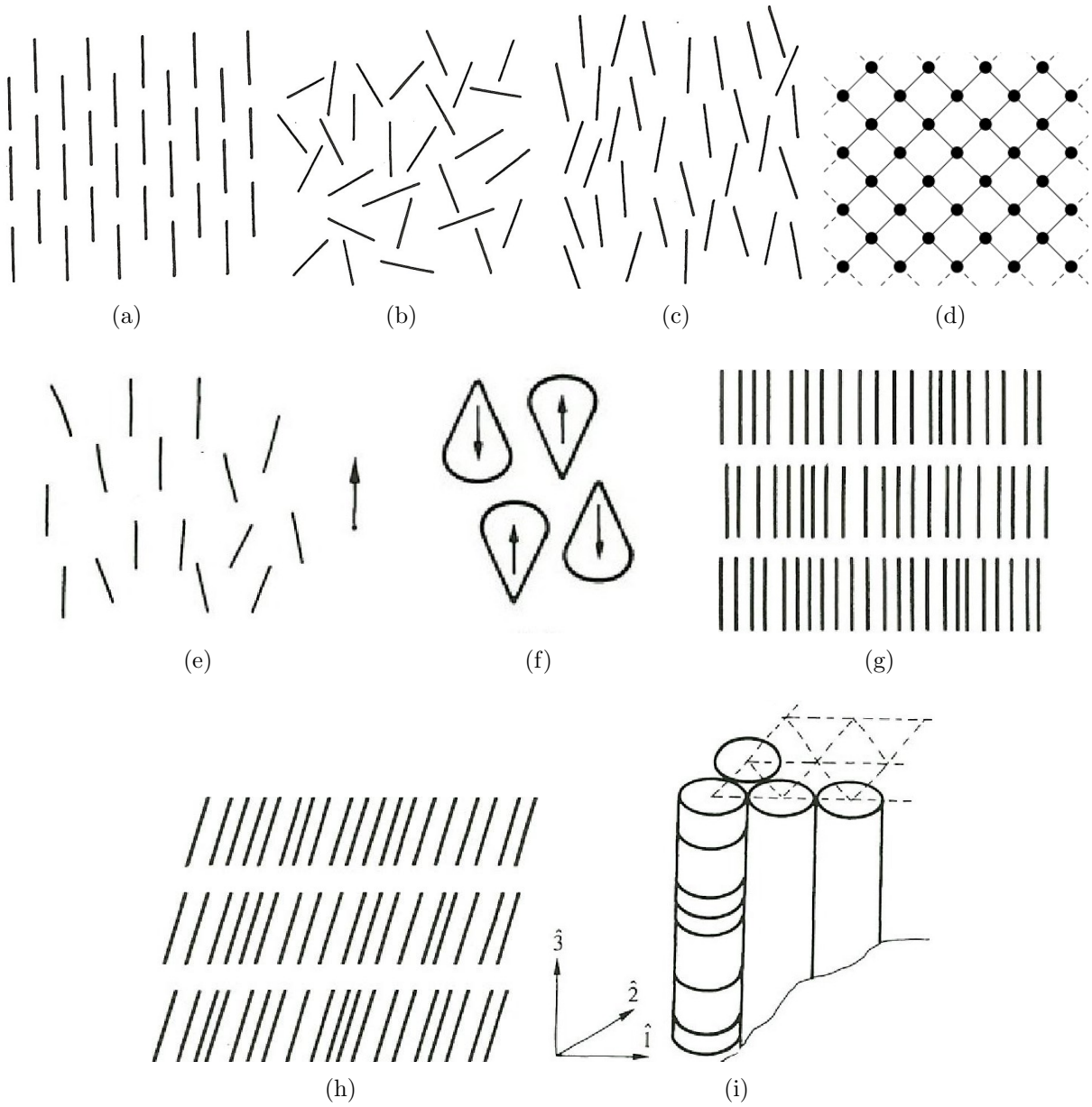

Figure 1.2: Schematics of different phases of matter: (a) crystal, (b) isotropic, (c) orientational order, (d) positional order, (e) nematic order, (f) dipole, (g) smectic A, (h) smectic-C, and (i) columnar. (a-c) taken from ref. [2], (d-f) from ref. [3], (g-h) taken from ref.[2], and (i) taken from ref. [3].

liquid whose molecules are oriented in a preferred direction known as the nematic director, represented by a unit vector $\boldsymbol{n}$. The nematic phase breaks rotational isotropy but not transitional invariance, as shown in Figure 1.2c. Rotations about an axis parallel to $\boldsymbol{n}$ leave the nematic phase unchanged, whereas rotations about axes perpendicular to $\vec{n}$ do not [10]. The nematic director $\boldsymbol{n}$ is also referred to as long range order because it shows overall tendency of material particles to be parallel to a preferred axis. This direction is arbitrary in space and may be imposed by external forces such as boundary forces, geometry and thermal fluctuations which can vary inside the material. In nematics $\boldsymbol{n}$ and $-\boldsymbol{n}$ are the same. For instance, if the individual molecules carry a permanent electric dipole, there are just as many dipoles up as there are dipoles down [3] as shown in Figure 1.2f.

Smectics. This class of LC phases possess, in addition to nematic order, one dimensional positional order in three dimensional space. Restricting order to be one-dimensional allows two degrees of freedom; from a mathematical point of view this means they can form a 2D subspace in 3D space. Therefore smectics are made of multiple layers with the molecule centre of mass, on average within the layer, but randomly positioned throughout. Thus each layer in a smectic phase is like a two-dimensional nematic. Since smectics are stratified, different ordering can exist within layers which results in different smectic phases. Among them two phases are most common: smectic-A and smectic-C. In the smectic-A mesophase, molecules are oriented parallel to the layer normal and the spacing between layers is almost equal to the molecular length. In the smectic-C mesophase, the nematic director is tilted relative to the layer normal, therefore they have less symmetry than the smectic-A mesophase [10].

Columnar. The columnar class of liquid crystals has the highest degree of positional order, two, and is one degree lower than crystal ordering. They form a two-dimensional lattice while maintaining liquid-like order in the third dimension to form columns of one-dimensional liquids. Because building blocks of this phase are mainly disc-like molecules they are also named discotic phases. Based on the structure of two dimensional lattice, different types can be distinguished: rectangular, oblique, and hexagonal phases (Figure 1.2)i.

1.3 Nucleation

As discussed in the previous sections, liquid crystals are mesophases and exhibit phase transition from the liquid-to-liquid crystalline state. This transition is first-order and is

initiated through nucleation, similar to the liquid to solid transition. It is because of this nucleation process that a disordered/liquid material can be subjected to undercooling without turning into a solid, in that a nucleus must form and grow to initiate the transition. Both of these mechanisms are dependent on the degree of undercooling, therefore the morphology of the material is temperature-dependant. Based on the initial state of nucleation, two different types can be distinguished. If this process happens inside the original phase without participation of a secondary material, it is called homogeneous. But if an impurity or another material is involved, then it is called heterogeneous nucleation [11].

Homogeneous nucleation. In an undercooled liquid, thermal fluctuations result in the formation, growth, and decay of crystalline nuclei. These nuclei can be approximated by spheres of radius r. This increased order results in a decrease of the free energy, which is favourable from thermodynamic point of view. On the other hand, an interface is formed between the disordered and ordered phases which is elastic and stores energy. In fact, this interface is a grain boundary and is thermodynamically unstable. Therefore, there is competition between interface creation and ordering. This competition results in a critical radius r_c existing, such that if a nucleus is greater than r_c, it will grow otherwise it melts. While the crystalline phase is growing, the interface can change shape in order to decrease the elastic energy and produce defects within the crystal.

Heterogeneous nucleation. In this type, nucleation is induced by an external phase like an impurity or boundary wall, therefore it is an extrinsic process. Most LC devices are designed in such a way that nucleation happens at the boundary, because this is the only way that structure can be manipulated and controlled. Otherwise nucleation would be random and not practical for optical devices. Therefore we focus on nucleation initiated from boundary. There are two major mechanisms involved in surface alignment and molecular ordering at the interface. Physicochemical forces like hydrogen bonding and dipole-dipole forces play a main role in orienting material particles. The second mechanism is material elasticity and surface topology which can affect the surface orientation indirectly. Since intermolecular forces in liquid crystals are anisotropic, the phase is elastic and tends to orient its particles in such a way to minimize elastic forces. Thus, free energy in this phase depends on structure and curvature of the material in addition to temperature and pressure. If temperature and pressure are held constant then the substance would reorient itself in order to relax the stress caused by deformation, like an elastic material. If surface energy or interactions are large compared to elasticity, molecules close to the interface maintain a constant direction regardless of the magnitude of curvature. This case is referred to

as strong anchoring. On the other hand, when elasticity is comparable to surface free energy, the two mechanisms would affect the molecule direction at the surface. There is an easy axis due to surface interactions which would be the molecules direction if there was only one layer of the liquid crystal on the surface. But since molecules in the bulk of the material tend to align the surface layer in their direction in order to reduce curvature and structural energy, the equilibrium structure would be different. In fact, the boundary layer is like a spring which has a relaxed state when molecules are in easy or preferred direction and any distortion from this state needs work that must be stored as elastic energy. This type is called weak anchoring. Based on the preferred axis, both strong and weak anchoring are divided into homeotropic and planar.

Homeotropic anchoring involves the nematic orientation aligning paralell to the surface normal, but in planar anchoring molecules are orthogonal to the surface normal (parallel to the surface plane). Because of the fact that in weak anchoring molecules are fixed at the boundary, some degree of tilt from easy axis is allowed for both homeotropic and planar anchoring. The type of anchoring depends on chemistry of liquid crystal and surface. If molecules are polar, anchoring can be strong, otherwise it is weak. Different types of organic and inorganic materials can be used as coating on the surface to change the anchoring. Rubbing the solid surface can also cause the molecules to orient parallel to the surface.

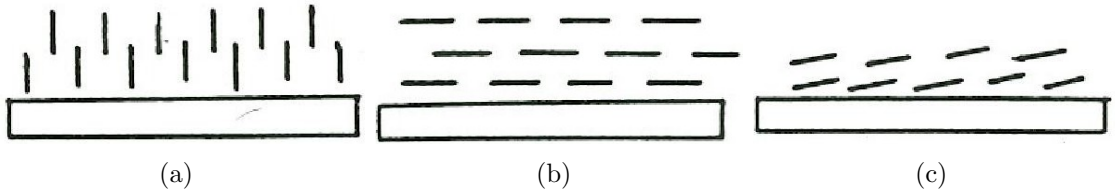

Figure 1.3: Schematics of different surface anchoring conditions: (a) homeotropic (b) planar, and (c) tilted anchoring. (a-c) taken from ref.[4].

1.4 Elasticity and Defects

As described earlier, liquid crystals share, to some extent, some properties with solids like order and elasticity. Even in a crystalline solid order is not complete and in some regions molecules do not conform the same ordering as the bulk of the material. For example, during phase transition if multiple nuclei form, grain boundaries form between the domains

that grow following their formation. Within these grain boundaries are defects in order, where ordering is either degenerate, or nonexistent (disordered). Defects can move inside the material under stress. In fact many materials are elastic because of their defects. In a relaxed solid, defects are at an equilibrium distance from each other. Stress causes them to move and interact with one another and with walls, therefore some sort of energy can be stored through deformation of the material. When stress is removed this energy and the forces associated with it result in defects translating to their original position. This is why solids like metals are flexible. The same phenomenon happens in liquid crystals. In LCs, a defect is defined as an area where the director field is degenerate and not well defined. In other words, if we consider molecular orientation as a vector field, defects are singularities within the field. Unlike solids, if an LC undergoes large deformations it does not break, but instead it forms more defects and keeps its structural integrity because it is also liquid-like. Formation, position and shape of defects depend on different parameters such as temperature, geometry of the domain, boundary conditions, elasticity of the material and initial state of substance. Since the director field is degenerate at defects, optical properties are different in defects. In many applications of LCs a very well ordered domain is required to result in a uniform optical axis.

Classification of defects is based on the amount of distortion that is present in their vicinity. Streamlines of the director field can converge or diverge at defects. This means there are rapid changes in direction and causes non-smooth rotation at defect points. Therefore defects are not analytical from mathematical point of view. In order to quantize the distortion, magnitude of rotation at defect is considered as a measure. Rotation is defined as change in polar angle of the director field over a closed curved around a point,

$$\Delta\theta = \oint_C d\theta \tag{1.1}$$

As long as the director is defined and continuous, θ can be found and it will be analytical and continuous,

$$\theta = \arccos(\vec{n} \cdot \vec{e}_1) \tag{1.2}$$

According to Green's Theorem, this line integral over a closed curve can be transformed to a surface integral,

$$\oint_C d\theta = \oint_C \nabla\theta \cdot d\vec{r} = \iint_D (\frac{\partial \nabla\theta_y}{\partial x} - \frac{\partial \nabla\theta_x}{\partial y}) dA \tag{1.3}$$

At regular points the integral would be zero because the two terms inside the double integral are equal. But if the curve encloses a singular point, gradients would not be defined

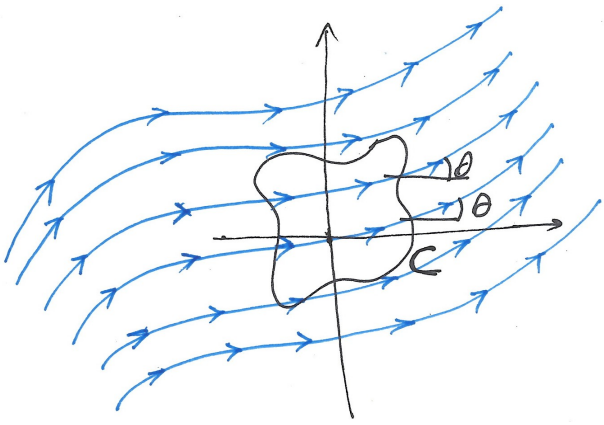

Figure 1.4: Rotation integral evaluated in a director field.

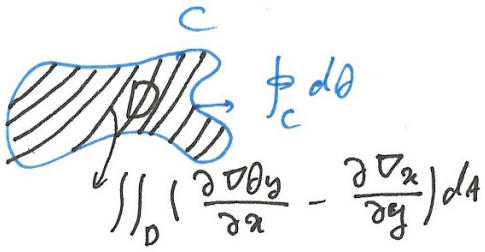

Figure 1.5: Green's integral theorem.

at the point and the integral would not be zero. Thus, this expression can identify regions that contain defects and distinguish them from well-ordered regions. Choosing a curve around a singular point in a vector field and traversing it, after a complete loop we reach to the same vector as starting point. Because $\Delta\theta$ shows difference between polar angles of start and end points, on a closed curve it has to be equal to a multiple of 2π. So at some defects the integral would evaluate to 2π. As discussed earlier, liquid crystals are mostly made of rod-like molecules and $\vec{n} = -\vec{n}$. For this reason, $\Delta\theta$ can take odd multiples of π. We only consider the π and 2π cases because higher angles are rare.

$$\Delta\theta = 2m\pi = \begin{cases} \pm 2\pi \Longrightarrow m = \pm 1 \\ \pm\pi \Longrightarrow m = \pm\frac{1}{2} \\ 0 \Longrightarrow m = 0 \end{cases} \tag{1.4}$$

where m shows number of full rotations and $\frac{1}{2}$ corresponds to half rotation. Figure 1.6 and 1.7 shows each type of defect.

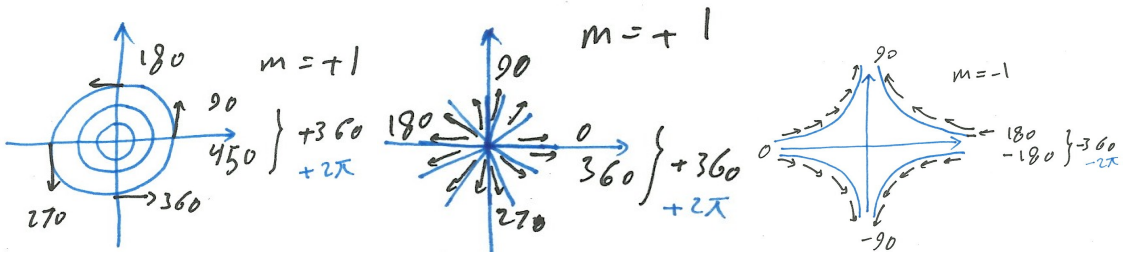

(a) $m = +1$ (b) $m = +1$ (c) $m = -1$

Figure 1.6: Schematic of a full rotation defect.

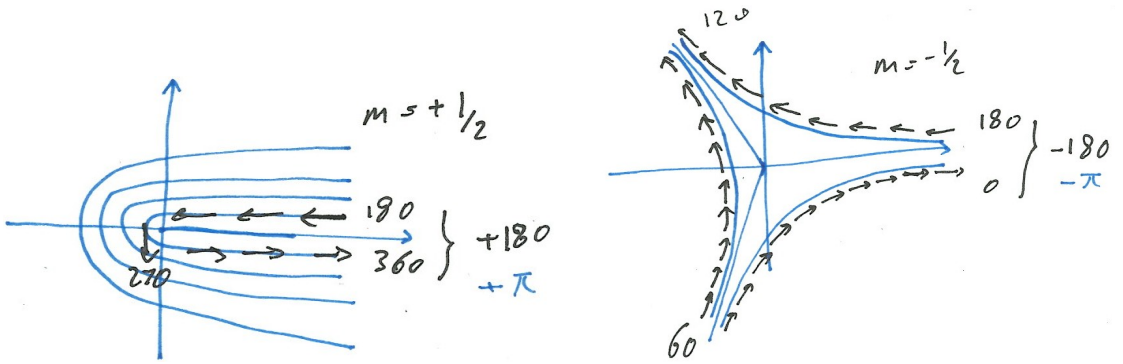

(a) $m = +\frac{1}{2}$ (b) $m = -\frac{1}{2}$

Figure 1.7: Schematic of a half rotation defect.

When $m = +1$, a defect causes the director field to have a full rotation around the defect. Therefore, both start and end vectors on a closed curve around a $+1$ defect have the same direction. Positive sign of m shows that with moving along a curve in positive trigonometric direction, which is counterclockwise, θ will increase. In the case of $m = -1$, a complete rotation exists, but θ will increase with rotating clockwise. $m = \pm\frac{1}{2}$ indicates that start and end vectors on a closed curve are in opposite direction of each other. It is clear that half rotation is the minimum distortion allowed for rod-like molecules, anything less will result in non-analytical and non-physical fields.

There are also other defect structures that result in the same rotation as the above defects, but they have not been observed in LC domains. It should be noted that the line integral does not depend on the shape of curve around the defect due to Green's Theorem.

Therefore, $\Delta\theta$ around a defect is constant.

$$\oint_{C1} d\theta = \oint_{C2} d\theta = \oint_{C3} d\theta \quad , \quad \oint_{C4} d\theta = 0 \tag{1.5}$$

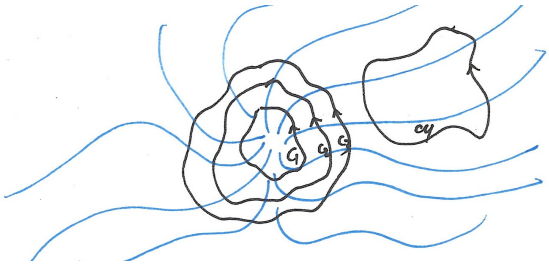

Figure 1.8: Schematic of different line integral around a defect.

1.5 Electric Fields and Applications

Since materials are composed of molecules, individual properties of molecules give rise to bulk properties. Most of LC molecules are not polar and do not maintain a constant dielectric anisotropy. But if an electric field is applied, electrons redistribute within the molecules because of forces created by the field. This migration gives rise to a local induced dipole along the molecular axis. Thus molecules experience different parallel and perpendicular forces with respect to the director. The result is a net torque on each particle that tends to orient them parallel to the field. If there is no competing force, all of the molecules would reorient their directions parallel to the field as shown in Figure 1.9. However, liquid crystals are elastic and also boundary conditions can impose force on the boundary layer and bulk.

The equilibrium structure would depend on all of the competing forces and defects can be affected by electric field (translation, formation, and annihilation). In practice, imposing an external field is the only way to manipulate the structure once the domain is formed. For real applications of liquid crystals, various orientation states of the domain are needed in order to produce different optical modes. The most simple and least costly way to manipulate these orientational states is through application of an electric field. LCDs are among the most significant liquid crystal deviecs which are composed of many micron-scale cubic cells filled with LC. An electric field is applied through two opposing faces of the cells to control the intensity of light and produce different colours.

Figure 1.9: Schematic of an LC molecule, or mesogen, rotating in response to an electric field.

Newer applications of LCs involve polymer dispersed-liquid crystals (PDLC) films which are sometimes called "smart" glass. They are, in fact, composite films composed of a thin layer of a glassy polymer matrix phase which encapsulates micron-scale LC domains. PDLC films enable tunable optical properties ranging from translucency to transparency which depends on alignment or texture of the encapsulated LC domains. Since electric fields can affect defects and LC texture, application of an appropriate field (strength and orientation) can be used to switch between the two modes.

Fabrication of a PDLC film involves mixing monomers and LC – polymerization results in the LC becoming immiscible with the polymer as molecular weight increases. This results in phase separation and a spatial distribution of spherical LC domains. PDLCs are inexpensive to produce in that they are formed naturally during the polymerization-induced phase separation process. Because PDLCs are inexpensive, they are of interest for large area applications such as windows and partitions.

1.6 Objectives

The presented research is a fundamental study on nematic domain confined within curved geometries. A theoretical approach is used to study nematic phase transition and dynamics in geometries presented in PDLCs – spheroids and ellipsoids with different boundary conditions. The study also includes external electric field effects (imposing and releasing the field) and defect response to the field.

Chapter 2

Theory

As discussed in the previous chapter, elasticity is considered as a contribution to the free energy in liquid crystals. Any form of deformation can result in elastic energy storage. This elastic energy is the driving force for change in the material structure in order to decrease the energy and stress. In addition to elasticity, in engineering applications the nematic texture is also governed by geometry of the domain and anchoring (boundary conditions).

Two parts of nematic order can be identified: short- and long-range order. First, short range order will be explained and quantified due to its relevance to both the nematic texture and thermodynamics. First-order phase transition is a gradual process which introduces multiple misoriented sub-domains (resulting from nucleation) into a nematic domain. This rarely results in uniformly oriented domains, although initially the case will be described where the nematic is everywhere aligned in the same direction. With this simplification, the degree to which molecules conform to the nematic director $\boldsymbol{n}$ is defined as the nematic scalar order parameter S. The values of S range from zero (disordered liquid) to one (perfect orientational order), while nematic LCs exhibit $S \in (0, 1)$. Figure 2.1 shows different configurations of an orientational distribution function which have the same director $\boldsymbol{n}$ but differ in the degree to which the molecules are distributed about $\boldsymbol{n}$. The nematic scalar order parameter S is a function of the angle between the director and each individual molecule and must increase as the angle decreases. Among different expressions, the second order Legendre polynomial of $\cos\theta$ is used [3],

$$S = \frac{1}{2} < (3\cos^2\theta - 1) >= \int_\Omega f(\theta)\frac{1}{2}(3\cos^2\theta - 1)d\Omega \tag{2.1}$$

where $<>$ represents the statistical average over molecules, $f(\theta)$ is the probability density

of finding a molecule with polar angle of θ from director, Ω is surface of a unit sphere around each point, and thus $d\Omega = \sin\theta d\theta d\phi$.

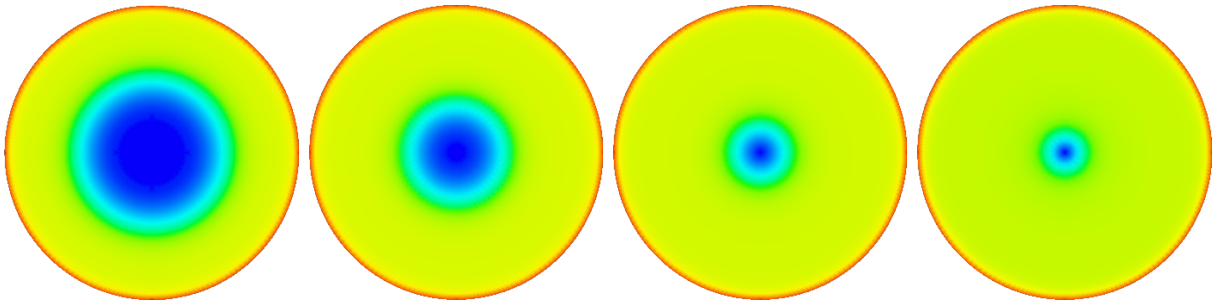

(a) (b) (c) (d)

Figure 2.1: Schematics of orientational distribution functions mapped from a half-sphere to a circle that show increasing S from (a) to (d). The surface color ranges from red (0) to blue (1) and represented the probability density of the molecular axis oriented in that area.

In a disordered/isotropic phase the molecules are randomly distributed and thus $f(\theta)$ does not depend on θ and is a constant. Average value of $\cos^2\theta$ is $\frac{1}{3}$ so in liquid $S = 0$. When all of molecules are oriented in one direction θ is 0 and S is 1. More details are given in the Appendix.

2.1 Frank's Elastic Model

While short-range order characterizes the degree to which the molecules conform to $\boldsymbol{n}$, long-range order simply refers to the nematic director $\boldsymbol{n}$. The nematic director can vary in space, and thus one approach to simplification of the dynamics of nematic order is to assume S is constant and neglect it. Frank proposed such a model [5] for nematics that orient their molecules parallel to one another at equilibrium if there is no boundary or external field with a different preferred axis. The theory is classified as nematic director theory and, as in solid mechanics, is based upon relation of a deformation $\nabla\boldsymbol{n}$ to elastic stress. In the nematic phase, curvature of the director imposes stress and torque. Therefore any elastic-continuum model in liquid crystals has to consider curvature as driving force for elastic energy storage and free energy change. Frank's model captures curvature through change of director at each point.

Frank proposed that local free energy density at each point of liquid crystal be function of $\nabla \boldsymbol{n}$. Local free energy f is per unit volume and thus the total free energy $F = \int f(x, y, z)dV$ may be minimized to approximate the equilibrium state of the nematic domain. Frank's model involves approximation of the free energy through truncating a Taylor's series expansion. Each partial derivative of director field component with respect to space is treated as independent variable and free energy is expanded around ground state which is uniform field everywhere and derivatives are equal to zero.

$$f(\frac{\partial n_i}{\partial x_j}, \frac{\partial^2 n_k}{\partial x_l \partial x_m}, \cdots) = f_0 \quad + \quad k_{ij}\frac{\partial n_i}{\partial x_j} \quad + \quad \frac{1}{2}k_{ijuw}\frac{\partial n_i}{\partial x_j}\frac{\partial n_u}{\partial x_w} \quad + \quad \text{H.O.T.} \tag{2.2}$$

where summation over repeated indices is assumed and f_0 refers to free energy of ground state. The coefficients are,

$$k_{ij} = \frac{\partial f}{\partial(\frac{\partial n_i}{\partial x_j})} \quad , \quad k_{ijuw} = \frac{\partial^2 f}{\partial(\frac{\partial n_i}{\partial x_j})\partial(\frac{\partial n_u}{\partial x_w})} \tag{2.3}$$

Frank's model includes terms only up to first derivatives which have physical interpretation in terms of deformation of the nematic director field as shown in Figure 2.2.

The Frank's elastic free energy must be independent of coordinate system. Thus if the coordinate system is rotated, the value of energy must be constant as long as the director field is unchanged. This allows significant simplification of the Taylor series expansion. In addition to coordinate system invariance, the symmetry of the nematic phase requires that free energy be invariant for $\boldsymbol{n} = -\boldsymbol{n}$. After grouping similar terms the vectorial form of free energy is,

$$f(n, \nabla n) = f_0 + \underbrace{\frac{1}{2}k_{11}(\nabla \cdot n)^2}_{Splay} + \underbrace{\frac{1}{2}k_{22}(n \cdot \nabla \times n)^2}_{Twist} + \underbrace{\frac{1}{2}k_{33}(n \times \nabla \times n)^2}_{Bend} \tag{2.4}$$

and the total free energy is found through integration of $f(\boldsymbol{n}, \nabla \boldsymbol{n})$ over the whole domain with proper boundary conditions.

$$F = \int_V f\big(n(x, y, z), \nabla n(x, y, z)\big)dV \quad + \quad \int_{\text{Domain Surface}} f_B(\text{Boundary Layer})dA \tag{2.5}$$

Total energy also includes energy associated with field structure on the surface that can be imposed by surrounding materials. In the next section a surface energy will be described which captures this energetic contribution. The equilibrium nematic texture is such that it

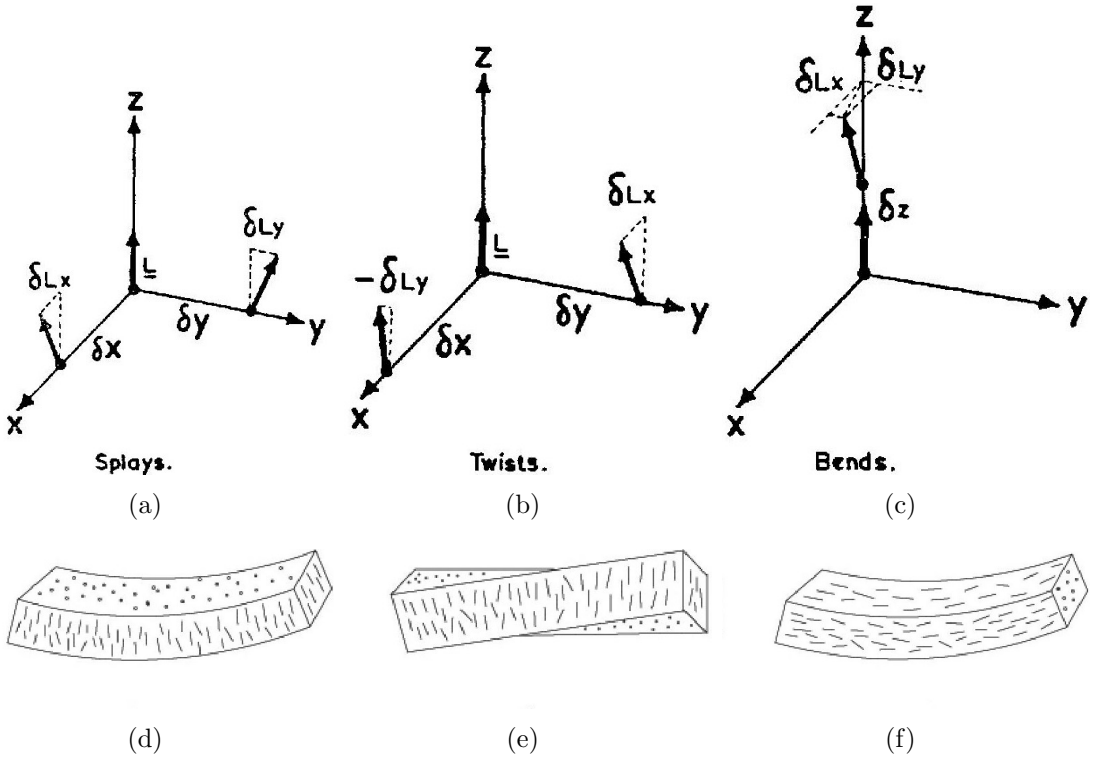

Figure 2.2: Modes of nematic director deformation in Frank's model. (a-f) taken from refs. [5, 6].

minimizes the total free energy, not the local energy. Total energy is a scalar and function of a vector field or a functional. Minimization of a functional involves the calculus of variations and will be discussed latter.

Since liquid crystals are susceptible to external fields because of their induced dielectric anisotropy, the director field would be influenced by both the natural preferred orientation of molecules and the field. Therefore these two forces compete and, depending on magnitude of field and elasticity of liquid crystal, one of them would be dominant and govern the structure. If the external field field strength is not large enough, it cannot affect the nematic texture and will leave the director field unchanged. There is a critical field strength that can change the orientation. This phenomenon is known as Freedericksz transition [2] and can be predicted by Frank's model. The electric field coupling term with director is,

$$\frac{1}{2}(\epsilon_{pa} - \epsilon_{pe})(n \cdot \vec{E}) \tag{2.6}$$

where $\epsilon_{\parallel}$ is electric permittivity parallel to director direction and $\epsilon_{\perp}$ is perpendicular to the director. In an anisotropic material these values differ which would result in a net torque resulting from misalignment with an external field.

One of the advantages of using Frank's model is that it is possible to find the critical field for each of the three deformation types. Conducting experiments under appropriate conditions enables the measurement of the critical field and subsequent prediction of elastic constants using Frank's theory. Figure 2.3 shows examples of these experimental conditions and the corresponding elastic constant that would be predicted.

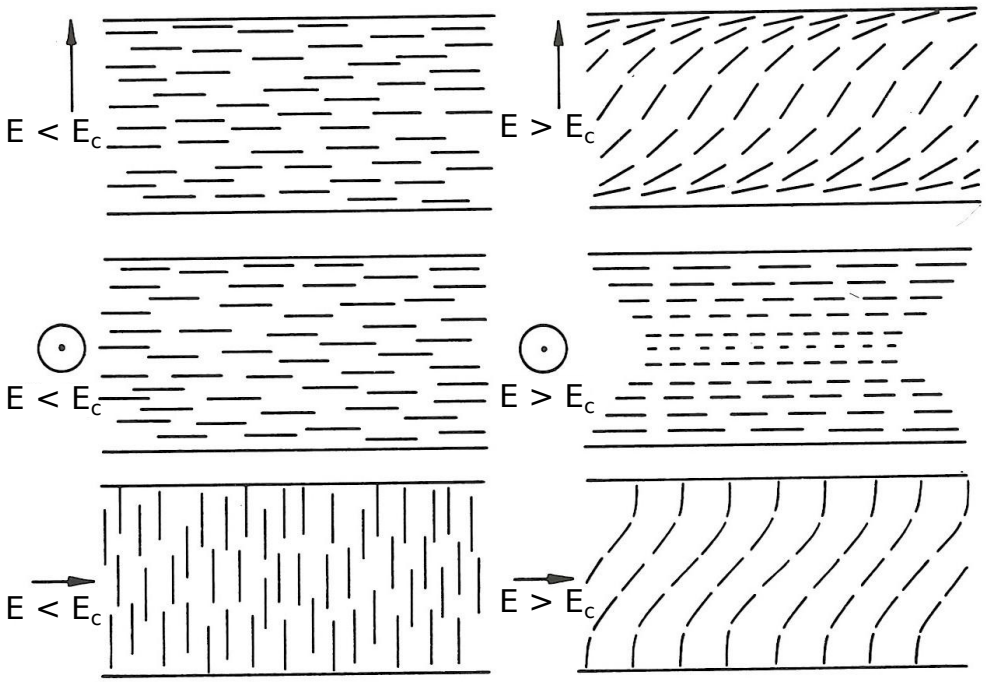

Figure 2.3: Different configurations to find Frank's elastic constants. Taken from ref. [2].

Frank's elastic model has two major limitations when applied to predict LC dynamics. Firstly, because the model only involves $\boldsymbol{n}$ and S is assumed constant, it cannot capture phase transition and is only applicable to nematic domains that are fully formed. Secondly, because defects are due to degeneracy in director field, this model cannot capture them in that the director field is not analytical and cannot be integrated through a functional. In fact, the minimizer of a functional can only predict smooth and analytical fields which can be integrated. Thus Frank's model is not appropriate for this study.

2.2 Landau-de Gennes Model

The Landau-de Gennes model for the nematic free energy [3] is expanded in terms of a tensorial order parameter that varies continuously from liquid phase to fully crystalline phase. This tensor is known as $\boldsymbol{Q}$ tensor and defined as below :

$$\boldsymbol{Q} = S\big(\mathbf{nn} - \frac{1}{3}\delta\big) + P(\mathbf{mm} - \mathbf{ll}) \tag{2.7}$$

where $\boldsymbol{nn}$ is the dyadic product of director with itself, $\boldsymbol{m}$ and $\boldsymbol{l}$ are perpendicular vectors to the director field which make a local orthogonal basis together with $\boldsymbol{n}$. The scalar P is another scalar order parameter which is called biaxial nematic order parameter. Nematics naturally tend to orient their molecules in one direction but sometimes due to boundary conditions and geometry, they might show simultaneous order in another direction perpendicular to $\boldsymbol{n}$. If $P = 0$ there is no preference between $\mathbf{m}$ & $\mathbf{l}$ directions. Then molecules are distributed evenly in the $\mathbf{ml}$ plane. If $P > 0$, molecules tend to orient in $\mathbf{m}$ direction more than $\mathbf{l}$ but $\mathbf{n}$ is still the major direction that molecules point. $\mathbf{l}$ is preferred direction in $\mathbf{ml}$ plane when $P < 0$.

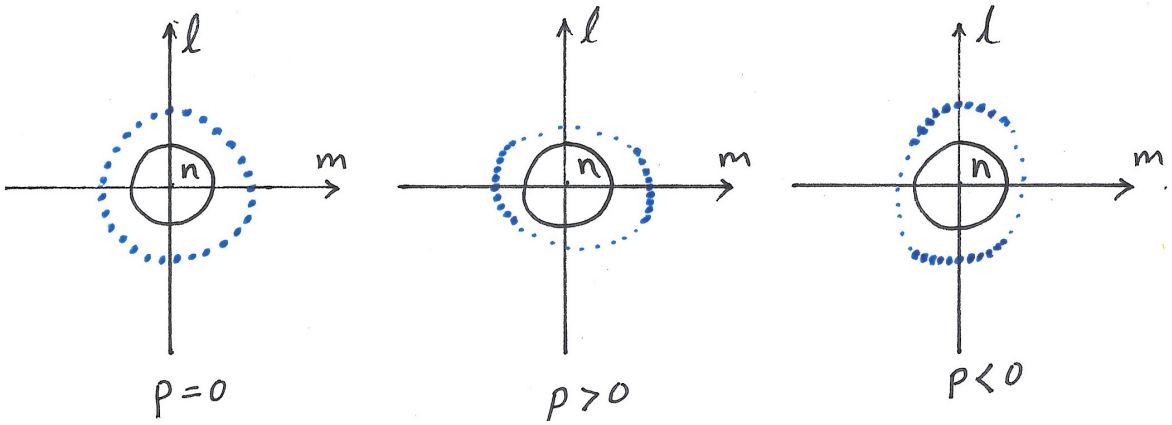

Figure 2.4: Schematics of orientational distribution functions for different values of P.

In the above expression for $\boldsymbol{Q}$, the tensor is defined through $\boldsymbol{n}$, S, etc. If the components of $\boldsymbol{Q}$ are known, for instance through a model or simulation, then $\boldsymbol{n}$,S, P can be found (see appendix).

The Landau-de Gennes model can capture both phase transition and elasticity, thus the free energy involves both $\boldsymbol{Q}$ and $\nabla\boldsymbol{Q}$ terms together in the expansion. Near a transition point, gradient terms are not significant and free energy mainly depends on $\boldsymbol{Q}$ itself, but as

a domain forms gradients can play an important role to reduce elastic energy and produce texture (coupled to boundary conditions and geometry).

$$f(Q,\nabla Q,\cdots) = f_{is} + \underbrace{\frac{1}{2}A(Q:Q) - \frac{1}{3}B(Q\cdot Q):Q + \frac{1}{4}C(Q:Q)^2 + \cdots}_{\text{Thermodynamics Terms}}$$

$$\underbrace{+\frac{1}{2}L_1\left(\nabla Q\vdots(\nabla Q)^T\right) + \frac{1}{2}L_2\left((\nabla\cdot Q)\cdot(\nabla\cdot Q)\right) + \frac{1}{2}L_3 Q:\left(\nabla Q:(\nabla Q)^T\right) + \cdots}_{\text{Elastic Terms}} \tag{2.8}$$

Because f is an infinite series, it must be truncated after a finite number of terms and the remaining non-zero coefficients must be approximated experimentally. In order to be able to find the coefficients, the first three terms from each of the free energy types, thermodynamic and elastic, are chosen (because $S < 1$ higher order terms are not significant).

In large domains where boundary effects are minimal, only thermodynamics terms exist, there is no gradient in the director field and biaxiality is zero. Therefore, for such domains,

$$f(Q) = f_{is} + \frac{1}{2}A(Q:Q) - \frac{1}{3}B(Q\cdot Q):Q + \frac{1}{4}C(Q:Q)^2 + \cdots \tag{2.9}$$

$$Q = S(\mathbf{nn} - \frac{1}{3}\delta) \Longrightarrow f = f_{is} + \frac{1}{3}AS^2 - \frac{2}{27}BS^3 + \frac{1}{9}CS^4 + \cdots \tag{2.10}$$

Thus f becomes a function of S only and does not vary in space. In order to minimize the total free energy, f itself has to be minimized which will result in a minimum for the total free energy functional. Each of the coefficients is a function of temperature but since near transition S is small, the effect of A is more than the effect of other terms and only this term is considered as a function of temperature. Above the transition temperature, S is 0 and free energy has to have a minimum at $S = 0$. Below the transition temperature S is positive. A simple form for A is $A = A_0(T - T_{NI})$ where T_{NI} is a second order transition temperature (in the absence of nucleation). In reality liquid crystalline phase transition dose not happen only at T_{NI} due to fluctuations in nematic order above the transition temperature. Even above this temperature, material goes through a meta-stable state where stability of nematic and isotropic phases is equal. This temperature is known as T_b, the bulk transition temperature. Between T_b and T_{NI} the nematic phase is more stable than the liquid phase. Above T_b and up to T_{SH}, upper stability limit, liquid phase is more stable than nematic phase. In temperatures higher than T_{SH} liquid is the only stable phase. Plots of free energy in these three different temperature regimes are shown in Figure 2.5.

Landau elastic constants can be evaluated through relationships to Frank's elastic constants. In the Landau-de Gennes model, elastic terms are not directly related to deformation types and it is difficult to measure them experimentally. Assuming S is constant in a

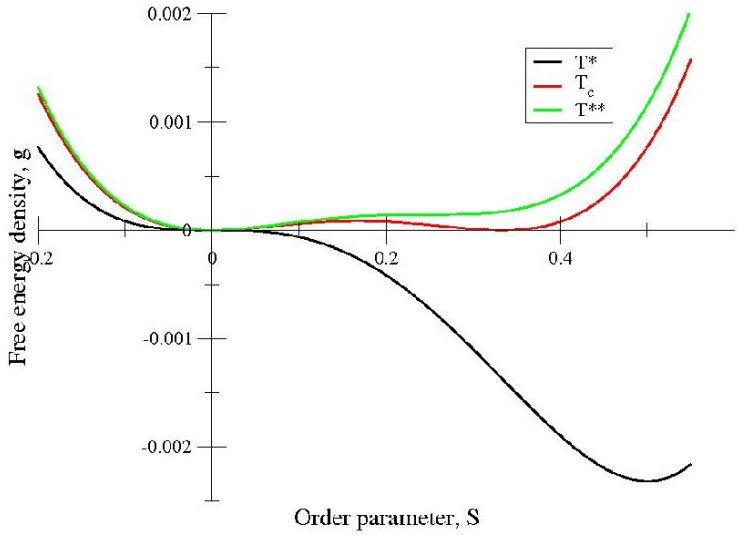

Figure 2.5: Free energy plot over different temperatures. Taken from ref. [6].

domain, then the gradient of $\boldsymbol{Q}$ can be connected to the gradient of n and elastic constants of both models can be related. The relations between L_i and K_{ij} are [12],

$$L_1 = \frac{3K_{22} - K_{11} + K_{33}}{6S_0^2} \tag{2.11}$$

$$L_2 = \frac{K_{11} - K_{22}}{S_0^2} \tag{2.12}$$

$$L_3 = \frac{K_{33} - K_{11}}{2S_0^3} \tag{2.13}$$

where S_0 is an average equilibrium scalar order parameter. In some liquid crystals K_{ii} values are equal that suggests bend, twist and splay have the same energy. With this assumption $L_2 = L_3 = 0$ and only $L_1 > 0$. Therefore the L_1 term can capture different modes of deformation.

In this work, the following form of free energy is used,

$$f = f_{is} + \frac{1}{2}A(Q:Q) - \frac{1}{3}B(Q\cdot Q):Q + \frac{1}{4}C(Q:Q)^2 + \frac{1}{2}L_1\left(\nabla Q \vdots (\nabla Q)^T\right) - \frac{\varepsilon_\circ}{8\pi}\left[\left(\frac{\varepsilon_\parallel + 2\varepsilon_\perp}{3}I + (\varepsilon_\parallel - \varepsilon_\perp)Q\right)\right] : EE \tag{2.14}$$

where E is the electric field vector and ε are the dielectric constants parallel and perpendicular to the director. Since the electric field tends to orient molecules along its direction, $\varepsilon_{\parallel}$ is greater than $\varepsilon_{\perp}$. Therefore the above free energy can be used for simulation of nematic domains in the presence of an electric field.

2.3 Surface Anchoring Energy

As discussed in the previous chapter, there are two major types of surface anchoring: homeotropic and planar. These correspond to anchoring orthogonal and parallel to the surface normal, respectively. In a more general way, surface energy can be classified depending on the "easy" or preferred axis. The easy axis can be a direction, $\boldsymbol{k}$, or a plane with a specified normal vector $\boldsymbol{k}$. In the first case deviation from the easy axis results in increase in the free energy. In the planar case deviation from normal vector decreases the free energy. If a spherical coordinate system is considered at each point of surface and θ as polar angle from $\boldsymbol{k}$ and ϕ as azimuthal angle around $\boldsymbol{k}$, surface energy should be function of θ and ϕ. Because most surfaces are isotropic, the free energy cannot depend on ϕ. Since $\boldsymbol{n}$ and $-\boldsymbol{n}$ are equal and molecules are non-polar, surface energy has to be an even function of θ . A siutable relationship can be found by adding even powers of $\cos\theta$ together which can be evaluated by $\boldsymbol{n} \cdot \boldsymbol{k}$.

$$\gamma = \sum_{i=1}^{\infty} \left(\sum_{j=1}^{\infty} C_{ij} S^j (\cos\theta)^{2i} \right) \tag{2.15}$$

the nematic scalar order S has a direct effect on surface energy because surface energy is also elastic. As the material approaches the liquid phase, the effect of surface anchoring vanishes, therefore γ is expanded in terms of S and θ. In order to use the Landau-de Gennes model, the surface energy has also to been derived in terms of $\boldsymbol{Q}$ [13],

$$\gamma = \alpha_1 Q : kk + \alpha_2 (Q : kk)^2 + \cdots + \beta_1 (Q \cdot Q) : kk + \beta_2 \left((Q \cdot Q) \cdot Q \right) : kk + \cdots \tag{2.16}$$

the largest term corresponding to the lowest power of $\cos\theta$ and S, which is the first term. In this work, the following expression is used for the surface energy,

$$\gamma = \alpha (\boldsymbol{Q} : \boldsymbol{kk}) \tag{2.17}$$

where α is the surface anchoring energy. When α is negative, $\boldsymbol{k}$ is the direction of easy axis and when it is positive $\boldsymbol{k}$ is the normal to the plane. It should be noted that this energy is per unit area and has to be integrated over the boundary surface to find the total surface energy.

Free Energy Minimizer

Up until now the free energy and boundary condition were defined mathematically through the Landau-de Gennes model. In order to predict a structure for the nematic domain, the free energy must be minimized. The free energy density, $f(Q, \nabla Q, \cdots)$, characterizes the elastic energy per volume for each point in a domain where $\boldsymbol{Q}$ can vary over space and time. The minimum of the free energy for each point is a uniform tensor field that has no spatial gradients since the material is nematic. Surface anchoring and geometry, in addition to nucleation, typically precludes the possibility of the nematic domain evolving to uniform ordering. In such cases, the boundary curvature penetrates into the domain, which results in a deformed nematic domain.

The first step in simulation is to find a $\boldsymbol{Q}$ field that minimizes the following total free energy:

$$F[Q] = \iiint_{\text{Bulk}} \left(\frac{1}{2}A(Q:Q) - \frac{1}{3}B(Q\cdot Q):Q + \frac{1}{4}C(Q:Q)^2 + \frac{1}{2}L_1\left(\nabla Q \vdots (\nabla Q)^T\right) \right.$$
$$\left. -\frac{\varepsilon_\circ}{8\pi}\left[\left(\frac{\varepsilon_\parallel + 2\varepsilon_\perp}{3}I + (\varepsilon_\parallel - \varepsilon_\perp)Q\right)\right] : EE \right) dV \quad + \quad \iint_{\text{Boundary}} \alpha(Q:kk)dA \tag{2.18}$$

The total free energy F of the domain (tensor field) is a functional. This means that $\boldsymbol{Q}$ is not an independent variable and cannot be differentiated in order to find differential changes of the functional around Q. Therefore a calculus relevant to functionals must be used that connects small changes in the function space, Q, to the independent and continuous variables. The idea of functional theory is to add an arbitrary function to the Q with a continuous and independent coefficient. Small changes to the Q field can be made by small changes of the coefficients. Therefore derivatives of a functional can defined through the coefficients [14].

A local minimum, or minimizer, of the functional is a $\boldsymbol{Q}$-tensor field such that any infinitesimal perturbation of the field results in a positive infinitesimal change of the functional. To find a minimizer, it should be assumed that it is something like $\widetilde{Q}$ and perturb it,

$$Q_{ij} = \widetilde{Q}_{ij} + \alpha_{ij} v_{ij} \tag{2.19}$$

where v_{ij} is any arbitrary function and α_{ij} are independent variables. If $\boldsymbol{Q}$ inside the functional is replaced with the above expression, then the functional would be a function of α_{ij} around $\widetilde{Q}$. Therefore, it can be minimized by taking derivatives with respect to α_{ij}

and setting them to zero. It should be noted that the answer must be independent of v_{ij}. The complete procedure is shown in the appendix. The result is that two sets of equations have to be zero, one comes from bulk integral and the other one from surface integral. The bulk equation is also known as the Euler-Lagrange equation of a functional and is the tensorial partial differential equation that has to be solved with the boundary condition coming from the minimization process,

$$\underbrace{\frac{\partial f}{\partial Q}-\nabla.\left(\frac{\partial f}{\partial\left(\nabla Q\right)}\right)=0}_{\text{Euler–Lagrange Equation}}\quad,\quad\underbrace{\frac{\partial\gamma}{\partial Q}+\frac{\partial f}{\partial\left(\nabla Q\right)}\cdot\vec{k}=0}_{\text{Boundary Condition}}\tag{2.20}$$

In the present work, a dynamical equation is needed, rather than a stationary one. In transport processes like momentum transport, the driving force is velocity gradient. The equilibrium state for velocity is when there is no gradient in the velocity field. Velocity gradients may be stabilised due to external forces like boundary conditions, pressure difference, and gravity. Momentum is always transported in the reverse direction of the gradient in order to unify the velocity field. In heat and mass transfer the driving force is gradient of temperature and chemical potential, respectively, and transfer direction opposes the gradient to reach a uniform equilibrium field. The same idea can used to make dynamical equation from Euler equation as driving force. In fact Euler equation is the first variation of the free energy functional [14] which is similar to the first derivative of a function (gradient). Thus the rate of change of $\boldsymbol{Q}$ is a proportional to Euler equation at any given $\boldsymbol{Q}$ field with a proportionality constant known as rotational viscosity.

$$\mu\frac{\partial Q}{\partial t}=\underbrace{-\left(\frac{\partial f}{\partial Q}-\nabla.\left(\frac{\partial f}{\partial\left(\nabla Q\right)}\right)\right)}_{M}\tag{2.21}$$

Due to the truncation of the free energy density, f, the Euler equation is not traceless and in order to be used for dynamics it should be made traceless since Q is traceless,

$$Trace(M)=b\sum_{k}\sum_{n}Q_{nk}Q_{kn}+\sum_{k}\frac{\varepsilon_{\circ}}{8\pi}(\varepsilon_{\parallel}-\varepsilon_{\perp})E_{k}E_{k}\tag{2.22}$$

$$\mu\frac{\partial Q_{ij}}{\partial t}=M_{ij}-\frac{1}{3}Trace(M)I\tag{2.23}$$

To generalize the equation, it is made dimensionless by defining dimensionless quantities,

$$\widetilde{T}=\frac{T}{T_{NI}}\quad,\quad X=\frac{x}{l}\quad,\quad\widetilde{t}=\frac{t}{\tau}\quad,\quad\tau=\frac{\mu}{a_{0}T_{NI}}\tag{2.24}$$

The dimensionless form of equation is given in the appendix.

2.4 Length Scales

In order to generalize the simulations, two different parameters are defined and used instead of actual values for external field effects and surface anchoring effects. The elastic term in the free energy functional is responsible for the deformation of the bulk and it tends to reorient the molecules such that a uniform domain is maintained.

$$\text{Elastic Term} : l_1(\nabla Q)\vdots(\nabla Q^T) \tag{2.25}$$

When the surface anchoring energy is on the order of this term, then the boundary texture and shape would penetrate into the bulk of the material. Therefore a length can be defined by comparing the two terms,

$$l_s \sim \frac{l_1 S}{2\alpha} \tag{2.26}$$

If l_s is small it means that the director can vary rapidly in order to compete with surface anchoring. Large values of l_s correspond to weak anchoring where the bulk texture dominates surface anchoring.

Like the surface penetration length scale, a length scale may be determined comparing electric field strength to nematic elastic energy term,

$$l_f \sim \sqrt{\frac{l_1 S}{\varepsilon E^2}} \tag{2.27}$$

which similar characterizes the effect of the external field with respect to the characteristic energy of elastic distortion of the nematic.

2.5 Numerical Methods

There are three main numerical methods to solve partial differential equations: finite difference, spectral methods, and finite elements. Finite difference is based on a local Taylor series expansion of the solution at each node of the domain. This method can capture any boundary condition but it is limited to simple geometries. In spectral methods, the solution is approximated by periodic functions which are global and defined over the whole domain. This method is fast and applicable to any boundary condition with high degree of convergence, but it is only applicable to the domains that can be transformed to rectangular geometry. On the other hand, finite elements can be used for any domain

shape and geometry, but boundary condition is limited to some forms. In this work, the finite element method is adopted because the geometry is curved.

In the finite element method, the domain is discretised into small domains and local functions are defined on each element of the domain. Local functions are non-zero on the elements which they belong to, but vanish on other elements or at least on most of other elements. The final solution is the sum of these local functions with a coefficient for each one. These coefficients must be found. Because any domain can be discretized into small sub-domains with regular shapes that are easy to work with and define local functions, this method is very popular for curved geometries.

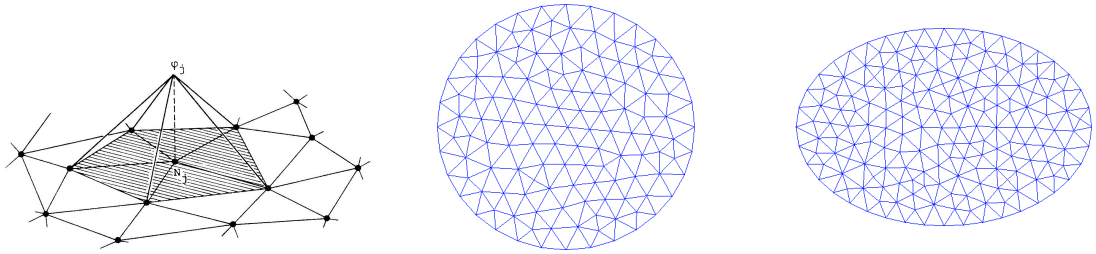

Figure 2.6: Schematics of (a) localized basis functions in the finite element method (taken from ref. [7]) (b) a meshed circular domain and (c) a meshed elliptic domain.

In most numerical methods, a differential equation is treated directly where the derivatives are approximated at each node and used to directly solve the equation. When a curved geometry is involved, it is difficult to find directional derivatives at boundary nodes and that is why many numerical methods are restricted to the rectangular or transformable to rectangular geometries. In order to solve this problem, the finite element method is based on integration rather than differentiation. In the finite element method a differential equation is turned into an equivalent integral or functional problem which has exactly the same solution. The integration is over the whole domain and also boundaries. Thus, instead of working with directional derivatives at boundary, an integration is added over the boundary. The idea is to multiply the differential equation by an arbitrary function from linear function space and then integrate over the whole domain.

$$\iiint_{\Omega} \left(\mu \frac{\partial Q}{\partial t} = - \left(aQ - b(Q \cdot Q) + c(Q : Q)Q - \frac{\varepsilon_{\circ}}{8\pi}(\varepsilon_{\parallel} - \varepsilon_{\perp})EE - l_1 \nabla^2 Q \right) \right) T d\Omega \tag{2.28}$$

$\forall T \in MS$ where Ω represents the domain or bulk and $MS = T : T$ is a piecewise continuous and bounded tensorial function on the domain. In the finite element method, boundary conditions are applied through the main equation and not separately, by using Green's

formula. This formula involves the Laplacian, which is over the domain, to the boundary and produces a directional derivative on it.

$$\iiint_{\Omega} T\nabla^2 Q d\Omega = \iint_{\Gamma} T\left(\nabla Q \cdot k\right) d\Gamma - \iiint_{\Omega} \nabla T \cdot \nabla Q d\Omega \tag{2.29}$$

where T is the surface normal and Γ is the boundary. Due to boundary condition that was derived previously, the boundary term can be simplified using,

$$\nabla Q \cdot k = -\frac{1}{l_1}\frac{\partial \gamma}{\partial Q} \qquad , \qquad \frac{\partial \gamma}{\partial Q} = \alpha k k \tag{2.30}$$

The boundary condition is applied through a surface integral in the main equation which involves a volume integral. The final finite element formulation of the PDE is:

$$\begin{aligned}\iiint_{\Omega} \mu \frac{\partial Q}{\partial t} T d\Omega = -\iiint_{\Omega} \Big(aQ - b(Q \cdot Q) + c(Q : Q)Q - \frac{\varepsilon_{\circ}}{8\pi}(\varepsilon_{\parallel} - \varepsilon_{\perp})EE\Big) T d\Omega \\ - \iiint_{\Omega} \left(\nabla T \cdot \nabla Q\right) d\Omega - \iint_{\Gamma} \frac{\alpha}{l_1} k k T d\Gamma\end{aligned} \tag{2.31}$$

As long as T belongs to the infinite dimensional function space, Q is the analytical solution to the equations. It is impossible to work with infinity in numerical methods. If the function space is restricted to a finite dimensional subspace of the whole space, then it is possible to find a numerical solution. When a subspace is chosen the solution is in fact the projection of the analytical solution to that subspace. In the finite element method, the solution is a linear combination of basis functions of the subspace. Coefficients can be found by applying the above integration on each basis function. In the simulations, second order Lagrangian basis functions are used.

Chapter 3

Formation and Structure of Ellipsoidal Nematic Domains

In this chapter, the material transformation process of elliptic cylindrical domains of a nematic liquid crystal (LC), initially in the disordered isotropic phase, are studied. The majority of manufacturing processes resulting in ellipsoidal confinement of an LC domain involve formation at temperatures above the upper stability limit of the LC phase. Upon quenching, a rapid cooling of the domain below the transition temperature, an isotropic-to-nematic transition occurs which forms the steady-state or "relaxed" nematic texture of the LC domain. This relaxed nematic texture directly affects the optical properties of materials and devices that are composed of LC domains, and thus is the first point of study.

3.1 Heterogeneous Nucleation and Growth

The steady-state of a cylindrical and spherical nematic domains has been well studied using Euler-Lagrange formulations of the Landau-de Gennes free energy for a range of diameters on the nanometer and micron scales [15, 16, 17, 18, 19, 20]. These studies have shown that the texture of these domains, consistent with the topology of a 2π rotation of the nematic alignment, has two characteristic types: radial and bipolar radial. Figures 3.1a-b show schematics of these two textures, where strong-anchoring is assumed. The radial texture is composed of a single +1 disclination defect in the centre of the domain. For a two-dimensional simulation (cylinder) this corresponds to a +1 line defect while for a three-dimensional simulation (sphere) this corresponds to a +1 point disclination. The bipolar

radial texture instead is composed of a pair of $+\frac{1}{2}$ disclinations, both of line character. In three-dimensional simulations of nematic spheres, a single $+\frac{1}{2}$ disclination *loop* is formed [18] which is topologically equivalent to a +1 point disclination. Sets of simulations have been performed for different LCs under the assumption of strong-anchoring which yield a relation between domain diameter, temperature and texture type (radial or bipolar radial). A schematic example of this data, or a *texture phase diagram*, is shown in Figure 3.1c, showing that the radial texture is only observed at small radii (with respect to the l_n) and high temperature (with respect to T_b).

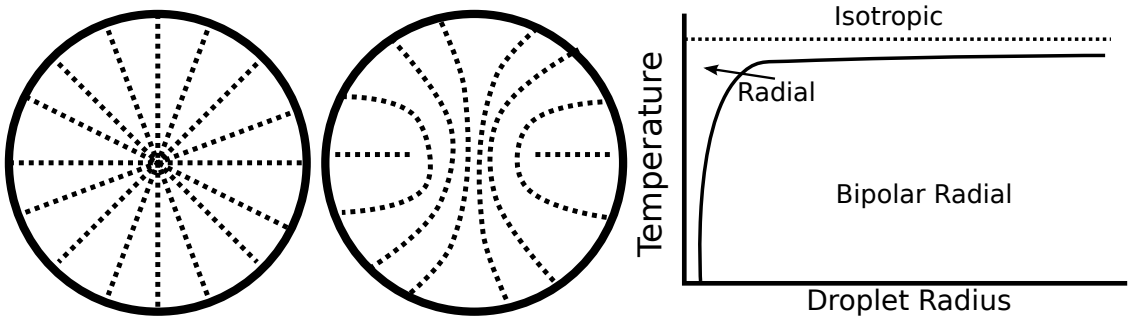

Figure 3.1: Schematics of the a) radial and b) bipolar radial textures of a cylindrical nematic domain; c) schematic plot of a texture phase diagram.

Simulations performed in this work are in two-dimensions, which correspond to cylindrical and elliptic cylindrical domains. Given that the majority of conditions result in a bipolar radial-type texture, these two-dimensional simulations provide some indication of the behaviour of full three-dimensional simulations of spheroids and ellipsoids. While this assumption does neglect the energetic cost of curvature of defect loops, the radial texture is actually not observable based upon simulation predictions with corrected dynamics (compared to past work).

In this work, the post-nucleation growth process is simulated using a time-dependent Landau-Ginzburg model for nematic phase transition and reorientation dynamics. This enables resolution of the dynamic growth process, given an assumption of the type of nucleation events that occur within the domain post-quench. An assumption is made that the nematic/solid interface enhances or promotes nematic order which results in a local surface transition (heterogeneous nucleation) preceding that of the bulk (homogeneous nucleation). Thus it is assumed that as the domain is quenched, an boundary layer exists that is nematic and growth proceeds from this layer. An example of this process is shown

in Figure 3.2, where the stable nematic boundary layer grows into the unstable isotropic bulk. The dynamics of the isotropic/nematic interface have been studied by Wincure and Rey [12] for the inverse problem, growth of a stable nematic domain in an unstable matrix phase. They have shown that the velocity of the interface is proportional to the difference in energy between the nematic and isotropic phase Δf and capillary forces:

$$\beta \boldsymbol{v} = C - \Delta F \tag{3.1}$$

where β is an effective viscosity term. Thus as the interface approaches the center of the domain, shown in Figures 3.2a-b, the capillary force grows proportional to $\frac{1}{r_i}$. As r_i approaches some critical radius $r_c \propto l_n$, $C \to \Delta F$ which results in a critical slowing of the interface growth. As shown in 3.2c, as this critical radius is approached, the growth process transitions to forming a nematic defect in the central region. This completes the initial transition process in that the domain is completely nematic, devoid of isotropic regions. Past results [16] show that following this transition process, there is a relaxation of the domain to either a radial or radial bipolar texture. The latter involves a splitting event of the +1 disclination, depending on the diameter and temperature of the domain shown in the texture phase diagram (Figure 3.1).

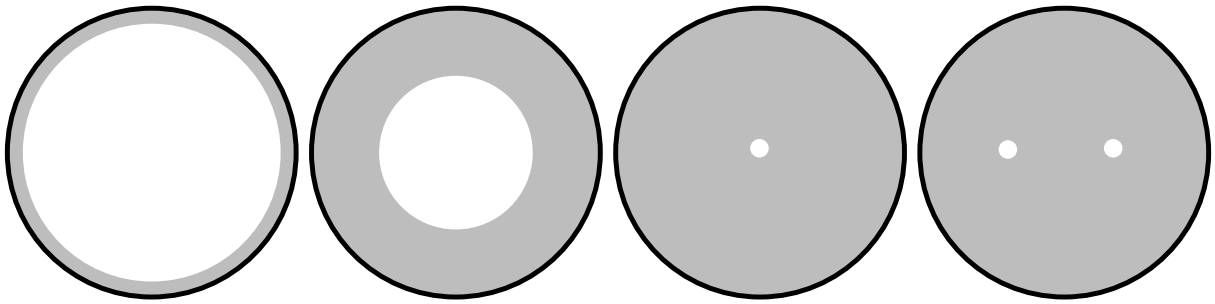

Figure 3.2: Schematics of the formation process: a) nucleation b) growth c) defect formation d) relaxation. Grey corresponds to the nematic phase and white to the disordered and biaxial phases.

Prior to simulation of elliptic cylinder domains, a study was first performed on circular cylindrical domains where $a \approx 1$, the ratio of long axis to the short axis, in order to validate the simulation method and compare to past results.

Table 3.1: Material parameters for 5CB.

a	1.4×10^5	$\frac{J}{m^3}$
b	1.8×10^6	$\frac{J}{m^3}$
c	3.6×10^6	$\frac{J}{m^3}$
l_1	3.0×10^{-12}	$\frac{J}{m}$
T_{NI}	307.2	K

3.2 Method and Simulation Conditions

Nematic reorientation dynamics simulations were performed using the dynamic partial differential equations and computational method description in Chapter 2. Model parameters were used that correspond to the pentyl-cyanobiphenyl [21] or 5CB liquid crystal compound, which has a bulk transition temperature of $307.2K$. These parameters are shown in Table 3.1, and the temperature of the quench was $307K$.

As opposed to past work, surface anchoring was assumed to be governed by the competition between the bulk nematic texture and surface anchoring energy. Thus a range of anchoring energies are used that correspond to strong to weak to free anchoring at the boundary with respect to a preferred orientational axis $\boldsymbol{k}$. This approach differs from the majority of past work which approximated strong anchoring through utilizing Dirichlet boundary conditions for the $\boldsymbol{Q}$ field. While this reduces the computational complexity of the simulation, the approximation fixes both alignment axis n, the degree of nematic ordering S, and the biaxiality at the interface β^2. In this work, none of these assumptions are made and anchoring strength is varied from weak to strong through changing the value of the surface penetration length l_s (Appendix). Simulations are performed under three surface anchoring conditions: strong anchoring $l_s << l_n$, moderate anchoring $l_s = l_n$, and weak anchoring $l_s >> l_n$.

In addition to anchoring strength, the shape of the domain was limited to elliptic cylindrical domains with aspect ratios either $a \approx 1$ (circular) or $a >> 1$ (elliptic). The aspect ratio was defined as the ratio of the long and short axes of the elliptic cross-section, d_l and d_s, respectively. The short axis is used as the scale of the domain, chosen such that $d_s >> l_n$, while the long axis is set to $d_l = ad_s$. The initial conditions of all simulations assume a boundary layer that is uniaxial and well-aligned with the preferred orientational

axis of the surface $\boldsymbol{k}(\theta)$, where θ is the polar angle of each surface point.

$$S(r,\theta) = S_b\left(\frac{r-\lambda R(\theta)}{R(\theta)-\lambda R(\theta)}\right) \qquad \text{For} \qquad \lambda R(\theta) < r < R(\theta) \tag{3.2}$$

and

$$S = 0 \qquad \text{For} \qquad 0 < r < \lambda R(\theta) \tag{3.3}$$

where S_b is the bulk/thermodynamic value of the uniaxial nematic order parameter at the boundary. It is assumed that S varies linearly over the boundary layer ranging from 0 to S_b at $r = \lambda R$ over a distance λ. In circular domains $R(\theta)$ is the radius of domain and it is a constant but for ellipse it the distance of surface point from origin and has the following form,

$$R(\theta) = \frac{a}{\sqrt{\cos^2\theta + a^2\sin^2\theta}} \tag{3.4}$$

The director field is set to be in radial direction for initial condition with $n = (a\cos(\theta), \sin(\theta))$ and,

$$Q^{int} = S_b\left(\frac{r-\lambda R(\theta)}{R(\theta)-\lambda R(\theta)}\right)\begin{pmatrix} a^2\cos^2(\theta)-\frac{1}{3} & a\cos(\theta)\sin(\theta) & 0 \\ a\cos(\theta)\sin(\theta) & \sin^2(\theta)-\frac{1}{3} & 0 \\ 0 & 0 & -\frac{1}{3}\end{pmatrix} \qquad \lambda R(\theta) < r < R(\theta) \tag{3.5}$$

$$Q^{int} = 0 \qquad\qquad 0 < r < \lambda R(\theta)$$

Simulations were performed using the finite element method for spatial derivative approximation with second order Lagrange basis function on a triangular mesh. Time-evolution was approximated using a second-order implicit trapezoidal rule method with a fixed time-step of $\tau = 50$ (dimensionless). Mesh-independence simulations were performed finding that a node density of $50\frac{node}{\mu m^2}$ was sufficient given an error tolerance of 10^{-8}.

The nematic reorientation dynamics prediction by these simulations involve many fundamental assumptions, summarized here:

1. **Hydrostatics** – phase transition and reorientation dynamics occur in the absence of flow.

2. **Fluctuations** – the effects of fluctuations are negligible [22].

3. **Heterogeneous nucleation** – the phase transition process is rapid such that the nucleation does not occur in the bulk and not likely to occur prior to defect formation.

4. **Higher Dimensions** – two-dimensional simulation of a elliptic cylinder domains provide insight into the dynamics of three-dimensional ellipsoidal domains.

Justifications for these assumptions, and associated limitations, will be addressed throughout the analysis.

3.3 Circular Nematic Domains, $a \approx 1$

3.3.1 Post-nucleation Domain Formation

Simulations of a circular domain were performed in order to validate and confirm the computational method with past results [16]. Figure 3.3 shows the evolution of a domain with $a = 1$ and $d = 200nm$ with moderate anchoring.

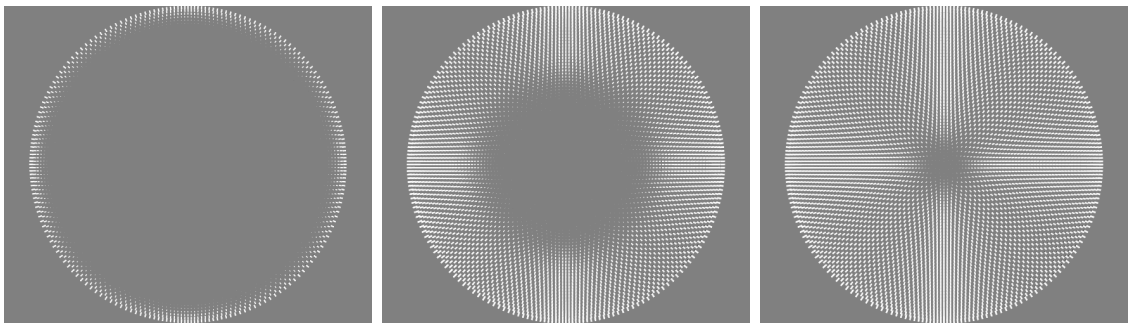

(a) (b) (c)

Figure 3.3: Evolution of domain without noise: (a) initial condition, (b) growth, and (c) defect formation.

Up to a critical radius the short range order (S) is approximately uniform throughout the domain. Within the domain centre, deviation from uniformity is observed where S (uniaxial order) decreases and P (biaxial order) increases which corresponds to an orientational defect or disclination. As P approaches S, the orientational order becomes degenerate with respect to the existince of a nematic director $\boldsymbol{n}$. In this case, due to the anchoring and geometry imposed on the nematic domain, the type of defect that is formed

is a +1 disclination, which corresponds to a full rotation of the nematic director around the defect core.

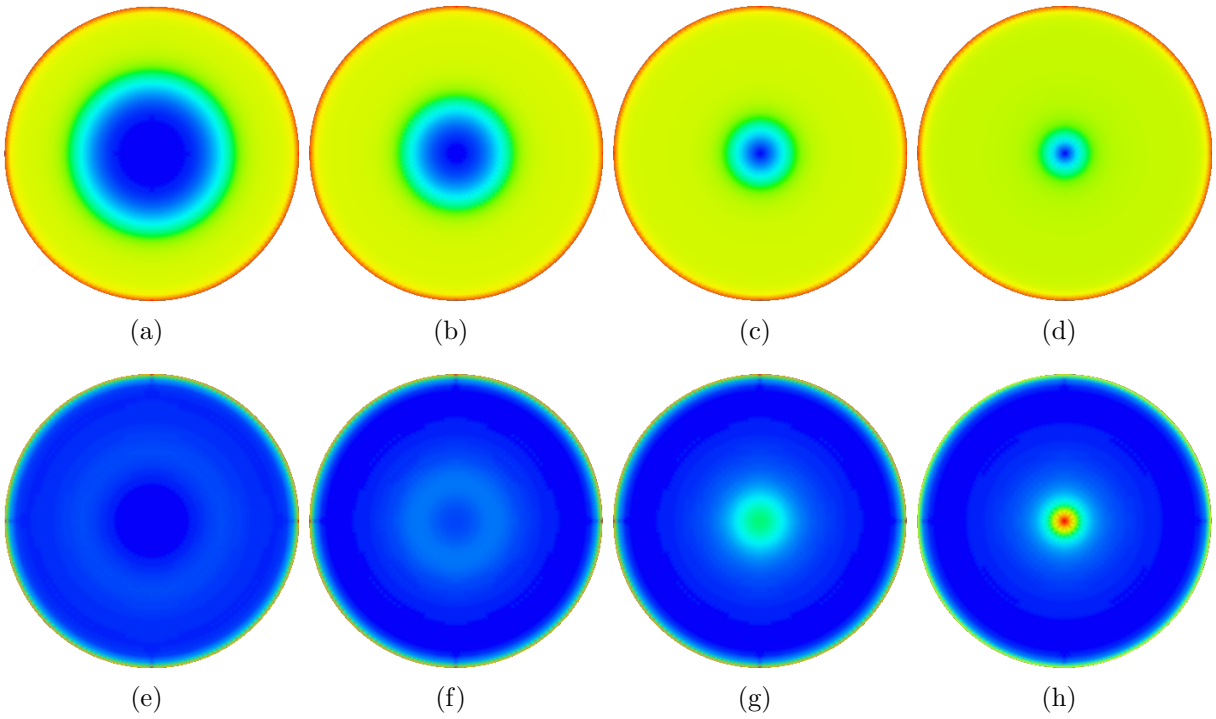

Figure 3.4: Surfaces of the (a-d) uniaxial nematic order parameter S and the (e-h) biaxial nematic order parameter profiles during the phase transition process.

As can be seen from above Figure 3.4, S and P are equal at the core when the defect is formed and the domain reaches steady-state. This equality means that the director is degenerate, it does not point only to one direction and a defect must exist.

This single defect formation is followed by splitting into a pair of $+\frac{1}{2}$ as time increases. The two defects have the same sign, hence there is a repulsive force between them which pushes the defect toward the boundary as shown in Figure 3.5 . The split happens due to core energy difference between +1 and $+\frac{1}{2}$ defects. The core energy associated with a defect is proportional to [23],

$$\pi K k^2 ln \frac{R}{r_c} \tag{3.6}$$

where k is defect strength, r_c is defect core radius and K is an elastic constant. With the

assumption of constant K and r_c, the energy of a $k = +1$ defect is twice as high as the energy of a pair of $k = +\frac{1}{2}$ defects. Thus, splitting results in a lower total energy.

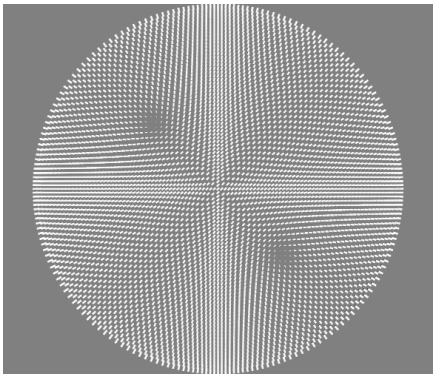

Figure 3.5: The steady-state nematic texture after defect splitting.

It was found that the time interval between +1 disclination formation and splitting did not converge during the mesh independence test. As the mesh density was increased, and simulation accuracy increased, the time to splitting was observed to increase which is shown in Figure 3.9.

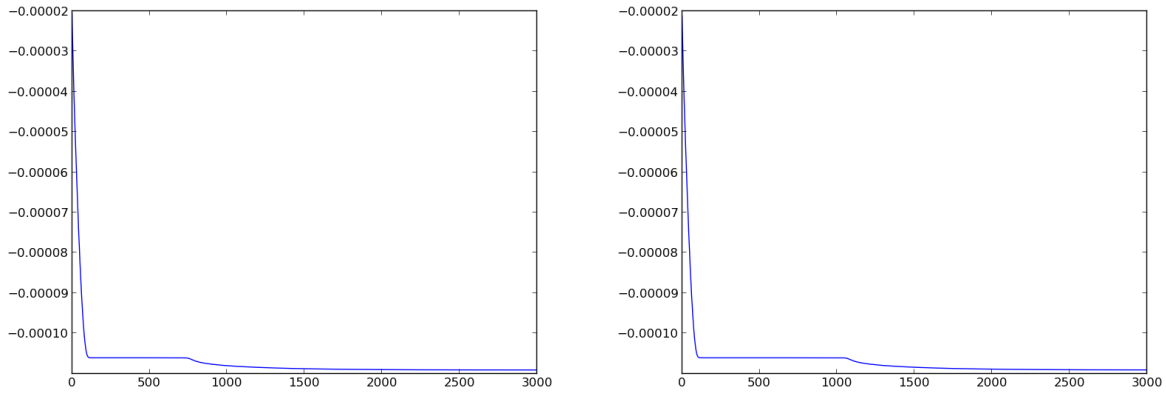

Figure 3.6: The dimensionless total free energy versus dimensionless time for two different mesh densities.

Initially, these results seemed contradictory with respect to past results [16], but after further analysis they were found to have a simple explanation. The dynamic equation

evolves the domain towards a solution which satisfies the Euler-Lagrange equation at steady state:

$$\frac{\partial \boldsymbol{Q}}{\partial \mathrm{t}} = -\frac{\delta F}{\delta \boldsymbol{Q}} \tag{3.7}$$

$$\text{Euler-Lagrange equation}: \ \frac{\delta F}{\delta \boldsymbol{Q}} = 0$$

but there are three classes of solutions which satisfy the Euler-Lagrange equation which are critical fields (maxima, minima, and saddles). The dynamic equation varies in the opposite direction of the fist variation of F which does not admit the possibility of reaching a local maximum, but saddle and local minima solutions are possible. Thus as the domain is evolved as governed by the dynamic equation, if a saddle is encountered the time derivative of $\boldsymbol{Q}$ approaches $\mathbf{0}$. Given that the governing equations are solved using approximate computational methods, approximation error will act as a series of perturbations to destabilize saddle solutions, but not local minima.

The same series of mesh independence simulations were performed, but now with an artificial noise added to $\boldsymbol{Q}$ field prior to +1 defect formation. Figure 3.7 shows the evolution of one of the simulations, which are qualitatively similar to those of the simulations without noise. With noise, the interval over which the defect splits was observed to decrease, which suggests that the texture with a +1 disclination is a saddle solution to the Euler-Lagrange equations. Additional simulations were performed at different domain length scales and it is found that the bipolar radial texture is a local minimum in all cases.

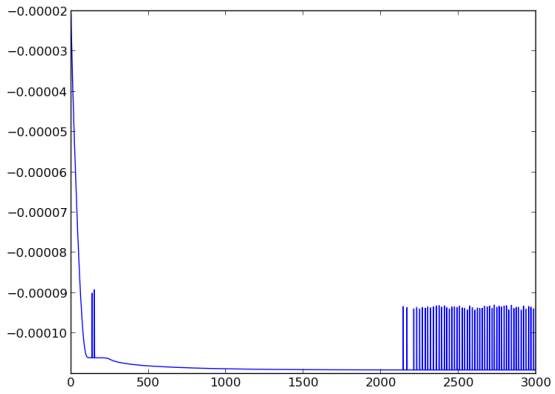

Figure 3.7: The dimensionless total free energy versus dimensionless time with noise.

This result implies that the use of the Landau-Ginzburg formulation for nematic reorientation dynamics must involve mesh independence test of *both* texture and dynamics. An interesting phenomenon that happens during the separation is that the direction of defects is different in different simulations. If the same code is performed multiple times, the polar position (angle) of the pair of defects would not be the same. This phenomenon cannot happen in deterministic equations. This behaviour can be described by the broken symmetry of a circle. If the equation were solved analytically over a circle, the result could not be a non-symmetric structure since the boundary and initial conditions are radially symmetric. Therefore, a single +1 defect would be a minimum for a circle. With numerical methods, it is impossible to get a represent and perfect circle due to meshing and round-off error

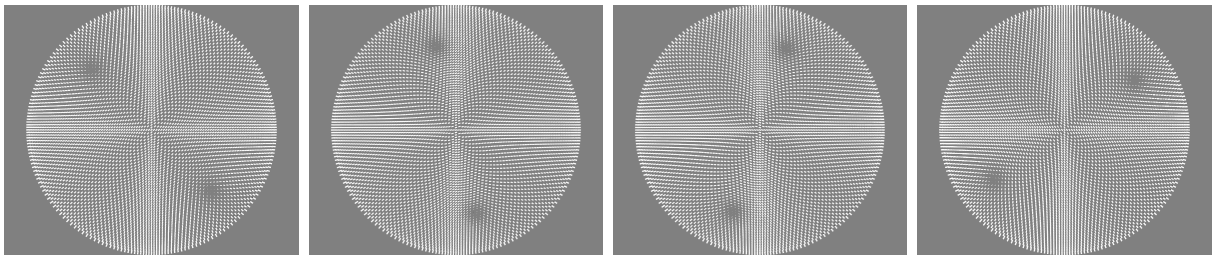

(a) (b) (c) (d)

Figure 3.8: Nematic textures from different simulations of the circular domain showing the degeneracy of the axis along which the defect split occurs.

In order to further understand this behaviour, simulations were performed with an aspect ratio slightly larger than one, $a = 1.05$. Texture evolution is qualitatively similar to $a = 1$ simulations, but even without the addition of artificial noise, the texture dynamics converged as a function of mesh density. This behaviour is attributed to symmetry of the simulations in a circular cylindrical domain. As the nematic interface grows into the centre of the domain it propagates with constant radial velocity at all points of the interface, as a result of the symmetry of the domain and initial condition. The driving force for the movement of the front is Δf (eqn. 3.1) but as the inner radius r_i decreases, capillary forces become large. For the perfectly symmetric case, in the absence of approximation error, there is no part of the highly curved interface that is more likely to grow inward. Any perturbation in the interface results in an aligned central region with broken symmetry; defect splitting then occurs on the axis orthogonal to the direction of alignment of the central region. For simulation of perfect circles, the presence of non-uniform mesh distributions and approximation error is the only possible source of pertubations, although unintended.

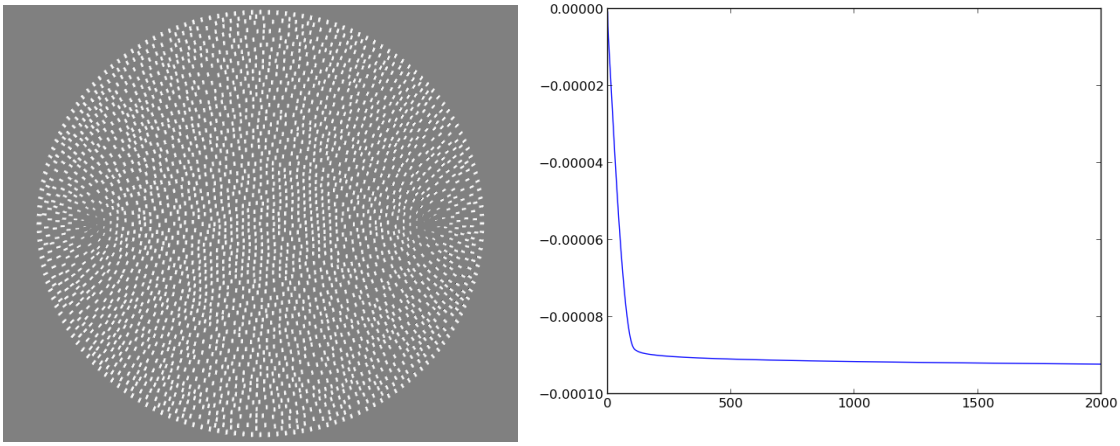

Figure 3.9: (a) Steady-state nematic texture for $a = 1.05$ and (b) the corresponding evolution of the dimensionless free energy.

For domains that are not perfectly radially symmetric, such as the simulations with $a = 1.05$, the portion of the interface that are in the vicinity of the short axis are exposed to lower interface curvature than regions along the long axis. Given that nucleation occurs uniformly along the boundary, there always exists a preferred axis along which $+\frac{1}{2}$ disclinations will form and lie along. Clearly this is not the case for $a = 1$ in that the texture in a domain may be rotated and result in a domain of the equivalent energy.

Thus, the introduction of an initial condition that lacks radial symmetry is one approach to using the Landau-Ginzburg formulation to predict convergent results. This does not preclude the possibility of encountering other scenarios where a saddle solution is present, and thus in all following simulations mesh independence studies were performed to show convergence of dynamics, in addition to steady-state state.

An alternate and more general approach would be to include thermal fluctuations through simulation of the dynamics using Langevin dynamics [24] which results in a stochastic PDE system [25, 22]. This requires the use of more complex computational methods for stochastic PDEs and significantly increases computational complexity.

3.3.2 Effect of Surface Anchoring Strength on Texture

The effect of surface anchoring strength was studied for a circular domain with $a = 1.05$ and $d = 200$nm. In all cases homeotropic anchoring was used with $\boldsymbol{k} = \boldsymbol{n_s}$ where $\boldsymbol{n}_s$

is the unit normal (outward) to the boundary. Simulations were performed for varying anchoring strengths $l_s = 1, 0.1, 0.01\mu m$ which are representative of weak, moderate, and strong anchoring, respectively. These values were based upon experimental characterization of these energies for different surfaces with 5CB [26].

Figure 3.10 shows steady-state textures resulting from simulations using these different anchoring strengths. Post-splitting of the +1 defect, the two $+\frac{1}{2}$ defects repel each other. As the defects approach the boundary, the surface stress increases proportionally to the anchoring energy. The surface anchoring energy competes with the bulk elastic energy, where the former resists deformation of the alignment at the boundary and the latter resists deformation in the bulk. Figure 3.10b-c show that as anchoring energy increases, disclination defects come to rest farther away from the bulk, comparing moderate to strong anchoring textures. In the case of weak anchoring, the bulk elastic stress overcomes the surface stress resulting in so-called "escape" of the disclination defects [27]. This escape phenomena results from large local deviations of the surface anchoring from the preferred direction. Subsequently, with the boundary conditions relaxed, the domain becomes well-aligned in the bulk along the axis orthogonal to the original defect trajectories (the major axis).

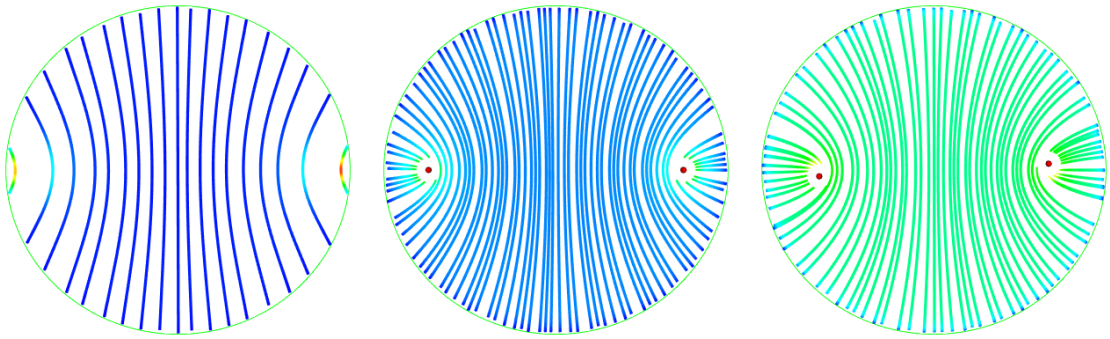

(a) (b) (c)

Figure 3.10: Nematic textures simulations with $a_r = 1.05$ and $d = 200nm$ with anchoring strength: (a) weak, (b) moderate, and (c) strong.

3.4 Ellipsoidal Nematic Domains, $a > 1$

In this part of the study, simulations of elliptic cylindrical domains were performed for a range of aspect ratios $a = \{2, 3, 4, 5\}$ and surface anchoring length scales $l_s = \{0.01, 0.1, 1.\mu m\}$

corresponding to weak, moderate, and strong. Once again, homeotropic anchoring was used along with heterogeneous nucleation as an initial condition. As was shown in the previous section, anchoring strength has a significant effect on the final ground state texture of the domain for circular cylindrical domains. In many manufacturing processes that form LC domains through phase separation, these domains are not perfectly circular [28, 29].

3.4.1 Post-nucleation Domain Formation

The growth process in the presence of anisotropy results in different interface dynamics compared to the circular case. The growth process of a domain with $a = 2$ is shown in Figure 3.11 and exhibits a qualitatively different formation process than for domains where $a \approx 1$. It is clear that interface regions closer to the major axis have greater curvature imposed by surface anchoring and geometry. Thus according to eqn. 3.1 they grow at a slower interface velocity compared to regions along the minor axis, which have lower curvature. As seen in Figure 3.11b, the rapid growth of the minor axis regions increases the region of high curvature along the major axis, which essential halts its growth early-on. Finally, 3.11c shows the domain fully transitioned into the the nematic phase with a pair of $+\frac{1}{2}$ disclinations located in regions of previously high curvature during the growth process.

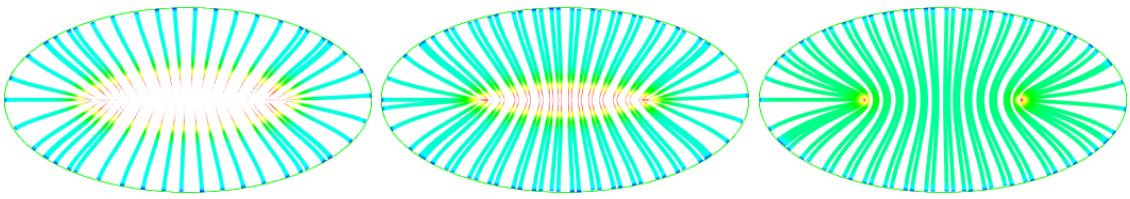

(a) (b) (c)

Figure 3.11: Evolution of domain with moderate anchoring and $a = 2$: (a) initial growth from post-nucleation, (b) interface along minor axis grows faster than along the major interface, (c) phase transition complete forming a nematic domain with $+\frac{1}{2}$ disclinations along the major axis.

Ground state textures for the range of aspect ratios with moderate anchoring are shown in Figure 3.12. The trend of increasing aspect ratio results in a decreasing radius of curvature in the boundary regions from each of the two foci to the ellipse boundary. Subsquently, the radius of curvature of the boundaries in between the two foci is decreasing and the overall curvature imposed by the boundary is localized to the focal region.

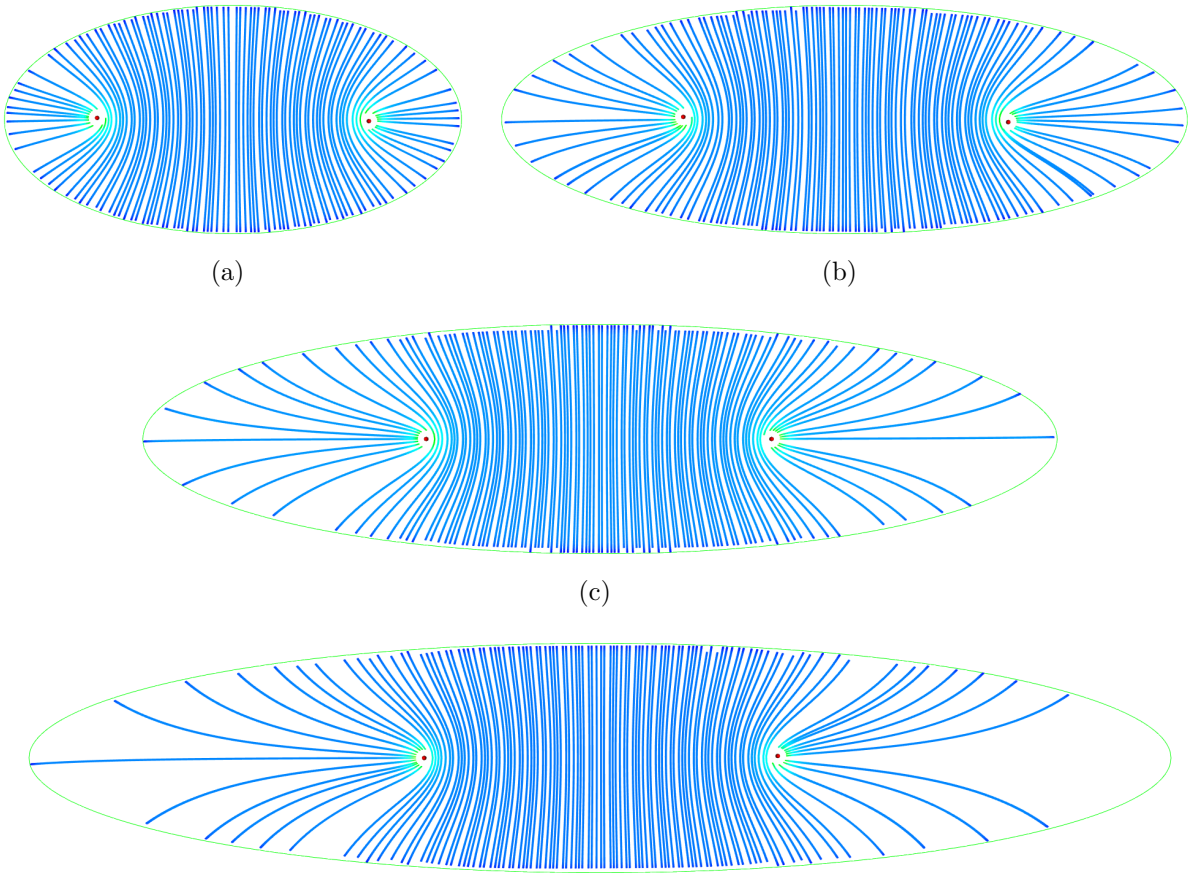

(a) (b) (c) (d)

Figure 3.12: Steady-state textures of domains with moderate anchoring and aspect ratio: (a) $a = 2$, (b) $a = 3$, (c) $a = 4$, (d) $a = 5$.

In order to understand the effect of domain eccentricity on the texture, the local curvature of an ellipse may used as an approximation for the curvature imposed, through surface anchoring, on the nematic alignment in the vicinity of the boundary. As the anchoring strength is increased, this approximation should be more accurate. Beginning with the parameter equation for an elliptic curve in $\mathbb{R}^2$ with major axis a and minor axis b,

$$\boldsymbol{r}(\theta) = \begin{bmatrix} a\cos\theta \\ b\sin\theta \end{bmatrix} \tag{3.8}$$

the mean curvature κ may be found for an arbritrary curve as follows,

$$|\kappa| = \frac{\|\boldsymbol{r}' \times \boldsymbol{r}'\|}{\|\boldsymbol{r}'\|^3} \tag{3.9}$$

where $\boldsymbol{r}' = \frac{\mathrm{d}\boldsymbol{r}}{\mathrm{d}\theta}$ and $\boldsymbol{r}'' = \frac{\mathrm{d}^2\boldsymbol{r}}{\mathrm{d}^2\theta}$. Substituting eqns. 3.8 into 3.9, the expression for the mean curvature of an ellipse is,

$$\kappa(\theta) = \frac{ab\left(\sin^2\theta + \cos^2\theta\right)}{\left(a^2\sin^2\theta + b^2\cos^2\theta\right)^{\frac{3}{2}}} \tag{3.10}$$

noting that for an ellipse $|\kappa(\theta)| = \kappa(\theta)$.

Figure 3.13 shows the mean curvature over a quadrant of an elliptic curve, which increasingly localizes in the focal region as aspect ratio is increased. This behaviour, although subtle, is observed in both the moderate and strong anchoring simulation, being more pronounced in the strong anchoring case. Disclination defects mediate the requirement of large curvature and gradients in nematic alignment between misaligned domains. Curvature imposed on the nematic alignment by the boundaries is increasingly localized to the focal areas of an ellipse as aspect ratio is increased, consistent with the topological properties of disclination defects. This also quantifies experimental observations [29] of the decrease in susceptibility to reorientation via external field that nematic domains exhibit which have increased aspect ratio.

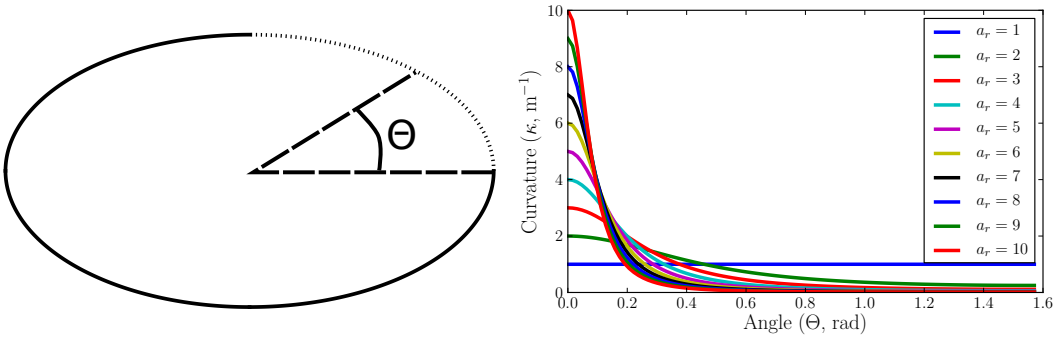

(a) (b)

Figure 3.13: (a) Schematic of the quadrant of an ellipse and (b) plot of curvature κ versus angle θ along the ellipse for increasing aspect ratio $a_r = \frac{a}{b}$.

3.4.2 Effect of Surface Anchoring Strength on Texture

The effect of surface anchoring strength was studied for the range of elliptic domain with $a_r = 2 \rightarrow 5$ and $b = 100$nm. In all cases homeotropic anchoring was used with $\boldsymbol{k} = \boldsymbol{n_s}$ where $\boldsymbol{n}_s$ is the unit normal (outward) to the boundary. Simulations were again performed for varying anchoring strengths $l_s = 1, 0.1, 0.01\mu m$ which are representative of weak, moderate, and strong anchoring, respectively.

As discussed in the previous section, the curvature of the boundary of an ellipse is increasingly localized as the aspect ratio is increased. Furthermore, as anchoring energy increases, the coupling of the alignment of the nematic at the boundary also increases. Thus, it is expected that under strong anchoring conditions the disclination defects present in the domain will have equilibrium positions closer to the focal regions along the major axis. Figure 3.14 shows ground state nematic textures for the $a_r = 5$ case for each of the three surface anchoring conditions: weak, moderate, and strong. The strong anchoring case behaves as expected; disclination defects are expelled from the bulk into the high curvature focal regions. Weak and moderate cases deviate substantially from the expected result imposed by surface anchoring. Clearly a competition exists between alignment preferred by surface anchoring (high curvature) and by the bulk (uniform/low curvature)

Surface anchoring is relaxed in order to accommodate a more aligned domain where bulk distribution of alignment deformation is well-distributed. For the strong anchoring case, surface anchoring is clearly dominant which promotes alignment in the central region of the ellipse. This is counterbalanced by a large amount of curvature in the focal regions with strong bulk alignment deformation.

Results for the remaining simulations with $a_r = 2 \rightarrow 4$ are shown in Figure 3.15. Results are consistent with previous discussion where two trends are observed:

1. Aspect ratio (weak/moderate anchoring) - as a_r is increased disclination position remains in the central region far from the high-curvature focal areas. Bulk alignment deformation is relatively well-distributed.

2. Aspect ratio (strong anchoring) - as a_r is increased disclination position remains in the focal region far from the low-curvature central areas. Bulk alignment is relatively uniform with large deformation in the focal region.

These trends suggest that, for elliptic cylindrical nematic domains, two general types of textures exist which are predominantly determined by surface anchoring strength and not aspect ratio. Instead of a gradual transition from an even-distributed deformation

of alignment to a well-aligned domain with localized extremes, there exists an effectively first-order transition between two states.

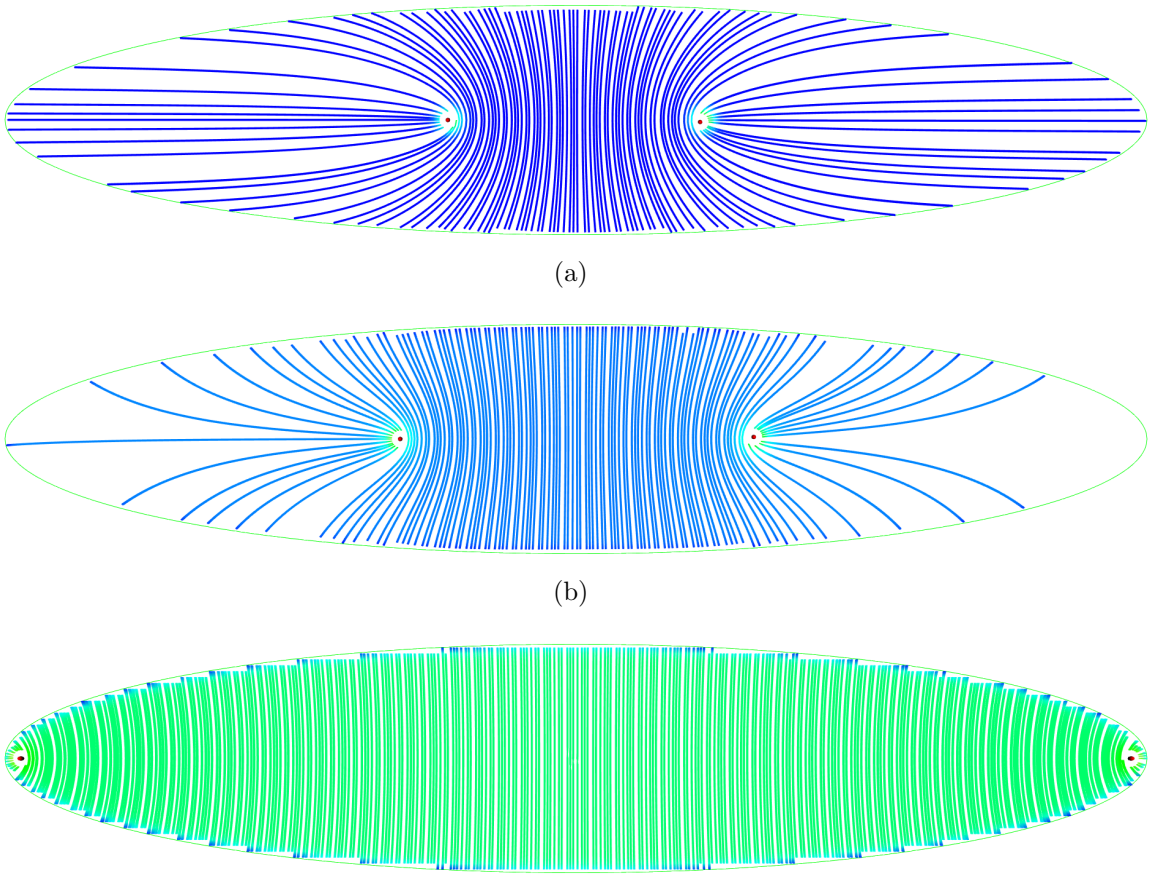

(a)

(b)

(c)

Figure 3.14: Steady-state textures of domains with $a_r = 5$ and (a) weak, (b) moderate, and (c) strong anchoring conditions.

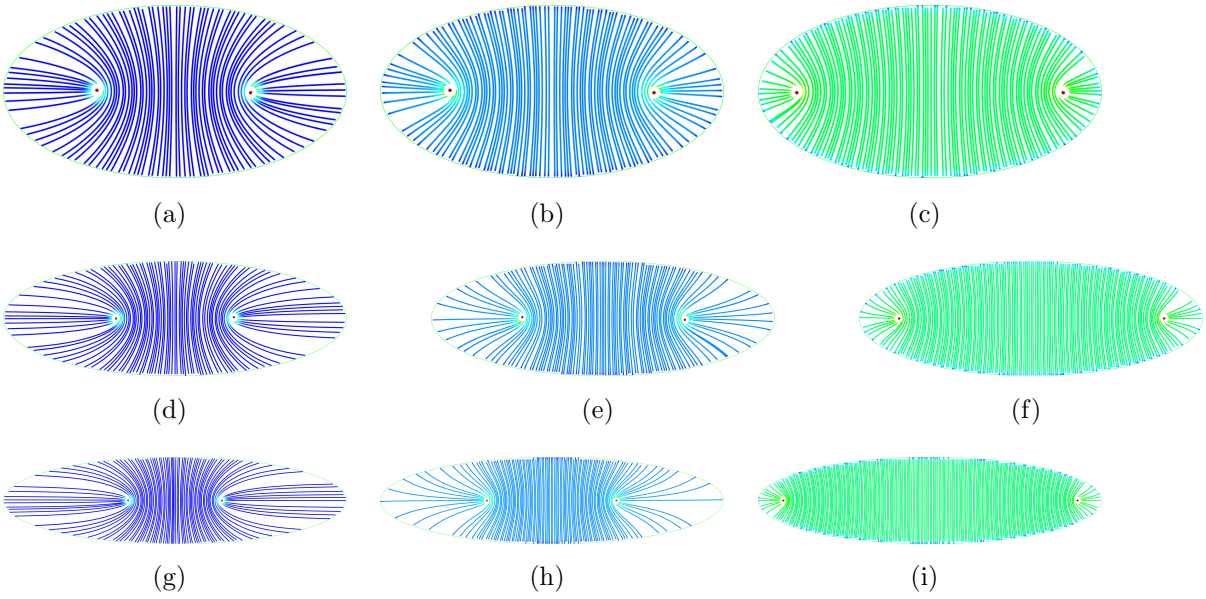

Figure 3.15: Ground state textures of domains with $a_r = 2, 3, 4$ and weak, moderate, and strong anchoring conditions.

Chapter 4

Field-switching Dynamics of Ellipsoidal Nematic Domains

In this chapter the effects of an external field on fully-formed elliptic cylinder domains of nematic liquid crystal (LC) are studied. Traditionally, external fields have been used to influence and "switch" liquid crystal domains from one state to another in order to affect the optical properties of the domain. Unlike these traditional applications, such as liquid crystal displays (LCDs), LC devices involving elliptic domains introduce topological defects in liquid crystal alignment which complicates their switching dynamics. Thus in this chapter the initially relaxed nematic textures are exposed to an external (electric) field and transition to a new steady-state. Both the realignment dynamics of the transition to this state, the new "driven" state texture, and subsequent relaxation once the external field is removed are the focus of this chapter.

4.1 Application of an External Field

In practice, the application of an electric field is more pragmatic than that of a magnetic field for LC devices. Under conditions typical of the formation of elliptic domains, the orientation of the domain with respect to the field varies. It is infeasible to perform simulations under all possible rotations of the domain, thus two sets of simulations were performed in orthogonal directions, as shown in Figure 4.1. It is assumed that the salient characteristics of the switching dynamics with fields in all possible directions are a combination of these two modes. As with surface anchoring, electric field strength (V/m^2) is varied from weak

to strong with respect to deformation energy of the LC domain. Simulations are performed using parameters which result in a range of values of the field penetration length scale,

$$l_f \sim \sqrt{\frac{l_1 S}{\varepsilon E^2}} \tag{4.1}$$

which, in this work, were 10nm (strong), 100nm, and $1\mu m$ (weak).

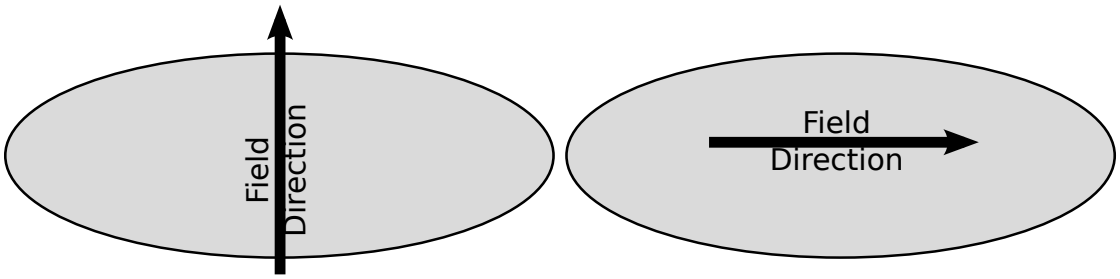

(a) (b)

Figure 4.1: Schematics of external field orientations along (a) the short axis and (b) the long axis of the elliptic domain.

Another significant assumption used in simulation of the application of an electric field is that coupling of the onset of the field and the polarization of the LC domain may be decoupled. The significance of this assumption may be elucidated for a simplified dielectric domain which is both uniform and isotropic. For such a domain, the polarization $\boldsymbol{P}$ (dipole moment per unit volume) is related to the applied electric field $\boldsymbol{E}$ as follows:

$$\boldsymbol{P} = \epsilon_0(1-\epsilon)\boldsymbol{E} \tag{4.2}$$

where ϵ_0 is the dielectric permitivity of vacuum and ϵ is the dielectric constant of the material. The onset of an electric field results in an effective current, or charge flux, called the polarization current:

$$\boldsymbol{j}_e = \frac{\mathrm{d}\boldsymbol{P}}{\mathrm{d}t} \tag{4.3}$$

This initial charge flux, in addition with other simplifications made for an ideal isotropic

dielectric medium, results in Maxwell's equations taking the form [30]:

$$\begin{aligned}
\nabla \cdot \boldsymbol{E} &= \nabla \cdot \boldsymbol{B} = 0 \\
\nabla \times \boldsymbol{E} &= -\frac{\partial \boldsymbol{B}}{\partial t} \\
\nabla \times \boldsymbol{B} &= \frac{\epsilon}{c^2}\frac{\partial \boldsymbol{E}}{\partial t}
\end{aligned} \tag{4.4}$$

where $c = (\epsilon_0 \mu_0)^{-\frac{1}{2}}$ and μ_0 is the magnetic permitivity of vacuum. Order-of-one scaling analysis [31] of Maxwell's equations 4.4 yields a characteristic timescale of the induced magnetic field:

$$\tau_m = \frac{E}{Bl} \tag{4.5}$$

where l is an imposed length scale of the domain, E and B are the magnitudes of the applied electric field and induced magnetic field, respectively. For the timescale of dynamics of the electric field:

$$\tau_e = \tau_m^{-1}\frac{\tau_m \epsilon l^2}{c^2} \tag{4.6}$$

From Section 2.3, the characteristic timescale of nematic alignment dynamics is:

$$\tau_n = \frac{\mu_r}{a_0 T_{NI}} \tag{4.7}$$

which is on the order of 10ns for low molecular mass liquid crystals such as 5CB [32]. Thus it is assumed in this work that $\tau_n >> \tau_m, \tau_e$, which is supported by much past work in the field on the effects of external applied fields [33, 17, 34].

The response of a nematic LC exposed to an external field is fundamentally dependent on the sign and magnitude of its dielectric anisotropy $\epsilon_a = \epsilon_\parallel - \epsilon_\perp$. The contribution to the free energy density of the nematic domain is,

$$f_e = -\frac{\epsilon_0}{8\pi}\left(\frac{1}{3}\left(\epsilon_\parallel + 2\epsilon_\perp\right)\boldsymbol{\delta} + \left(\epsilon_\parallel - \epsilon_\perp\right)\boldsymbol{Q}\right) : \boldsymbol{EE} \tag{4.8}$$

after substituting this into the nematic dynamic equation, the stress imparted on the nematic alignment through the external field is,

$$\sigma_e = \frac{\epsilon_0}{8\pi}\left(\epsilon_\parallel - \epsilon_\perp\right)\boldsymbol{EE} \tag{4.9}$$

which evolves the domain to minimize the contribution of the external field coupling in the free energy density as follows:

1. Positive dielectric anisotropy $\epsilon_{\parallel} - \epsilon_{\perp} > 0$ – nematic orientation aligns with respect to the external field $\boldsymbol{n} \parallel \boldsymbol{E}$.

2. Negative dielectric anisotropy $\epsilon_{\parallel} - \epsilon_{\perp} < 0$ – nematic orientation aligns orthogonally with respect to the external field $\boldsymbol{n} \perp \boldsymbol{E}$.

In this work only positive dielectric anisotropy is considered given that the majority of LC compounds and applications involve LCs of this character.

4.2 External Field – Minor Axis

The first simulation conditions that were studied involved application followed by release of an electric field along the minor axis of the elliptic cylindrical domains. Under these conditions, the bulk alignment of the domain is be enhanced by the external field which, based on observations from the previous chapter, requires translation of disclination defects further into the focal regions of the domain. In this sub-study, moderate anchoring conditions were used with a strong external field.

4.2.1 Application of External Field

Figure 4.2 shows the ground state in the presence of the external field, or "driven" state, for domains with aspect ratios from $a_r = 1 \rightarrow 5$ As expected, the external field increases bulk alignment which results in further movement of defects to the boundaries. In order for this to occur, the nematic alignment at the boundaries must relax with respect to the surface anchoring constraints.

Figure 4.5 shows the different components of the total free energy of the domain prior to and following application of the external field. Figure 4.5a shows that, upon application of the external field, the bulk component of the free energy rapidly increases due to the enhancement of short-range nematic order through coupling with the field term. Figure 4.5b show that the elastic component of the free energy decreases as the nematic alignment gradually increases uniform ordering in the direction of the external field. Subsequently, the surface free energy component, show in Figure 4.5c, shows an initial rapid decrease followed by a longer timescale net increase compared to the ground state. This initial rapid decrease is attributed to the "escape" of disclination defect from the domain resulting from increased alignment of the central region of the domain with the external field. The core region of the disclination defect exhibits a local depression in short-range nematic order,

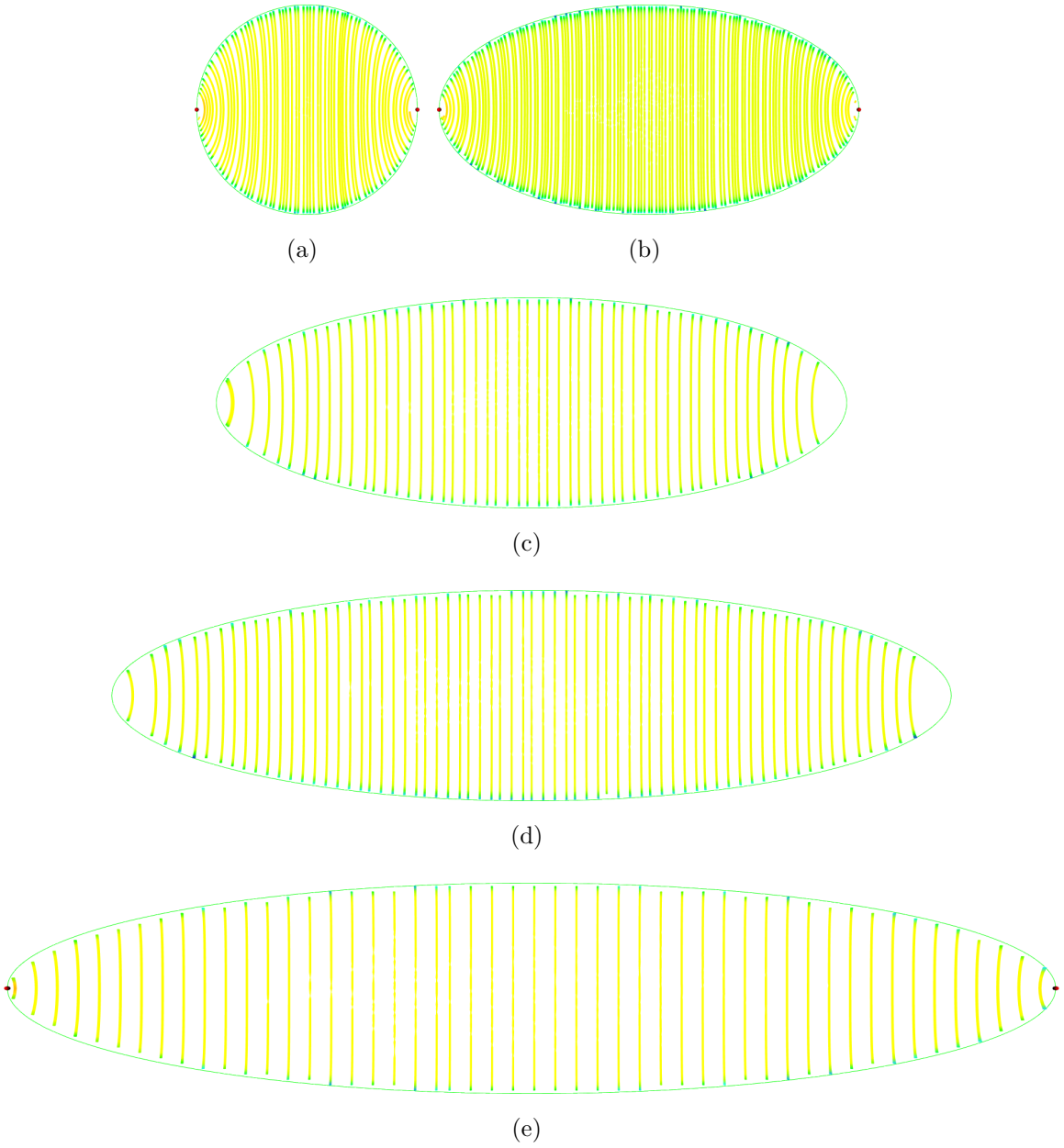

Figure 4.2: Hyperstreamline visualizations of driven state textures of domains with $a_r = 1 \rightarrow 5$ with strong anchoring and field conditions.

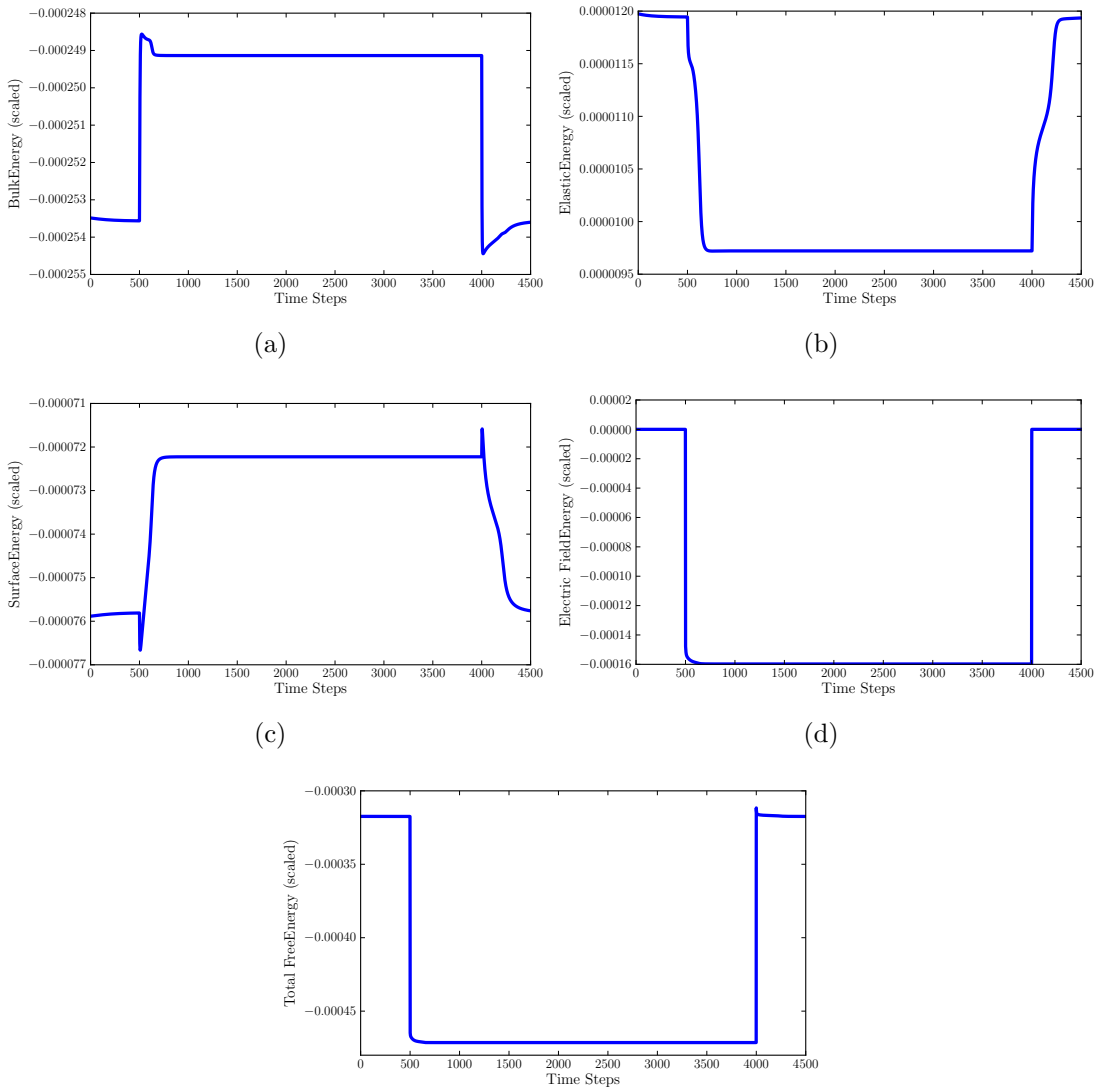

Figure 4.3: Free energy versus timestep for the simulation with $a_r = 3$ and the field along the short-axis: (a) bulk free energy, (b) elastic energy, (c) surface energy, (d) electric field energy, and (e) total free energy components.

given that the disclination core is biaxial, the surface free energy density may be expanded

as follows:

$$f_s(\boldsymbol{Q}) = \alpha \boldsymbol{Q} : \boldsymbol{k}\boldsymbol{k} = \alpha \left(S \left((\boldsymbol{n} \cdot \boldsymbol{k})^2 - \frac{1}{3} \right) + P(\boldsymbol{n} \cdot \boldsymbol{k})^2 \right) \tag{4.10}$$

given that $\alpha < 0$ and $\boldsymbol{n} \perp \boldsymbol{m}$, as the biaxial core approaches the boundary the contribution from the non-zero P will interact favorably with the surface anchoring of the curved boundary. Once the defect escapes, the predominantly uniaxial bulk with $\boldsymbol{n} \perp \boldsymbol{k}$ then interacts with the focal boundary region which increases the surface energy substantially.

Figure 4.5d shows the electric field component of the free energy which exhibits both short and long timescale dynamics as the short-range (S) and long-range($\boldsymbol{n}$) nematic order evolves to enhance and align with the field, respectively. The total free energy of the domain, shown in Figure 4.5e, shows an initial increase in the free energy resulting from the instantaneous application of the external field followed by both short and long timescale relaxations to the driven state.

4.2.2 Release of External Field

Figure 4.4 show ground state textures following relaxation of the nematic alignment after cessation of the electric field. The driven state is no longer stable and thus the domain evolves to a new steady-steate state, which is observed to different that the steady-state state resulting from phase transition of the domain (Chapter 3). In all cases, disclination defects reform within the domain but reside much closer to the focal boundary than in the initial ground state.

Figure 4.5 shows the different components of the total free energy of the domain prior to and following application of the external field. The relaxation process has similar features, with respect to the components of the free energy of the domain, as the reverse of the driven process. Initially, the enhanced short-range order of the domain results in a net decrease compared to the original driven state. This net decrease then relaxes towards a value close to the pre-driven state as the long-range elastic component increases driven by surface anchoring.

4.3 External Field – Major Axis

The next simulation conditions that were studied involved application and then release of an electric field along the long axis of the domain. The dynamics expected from these conditions are more complex in that the external field promotes orientation orthogonal

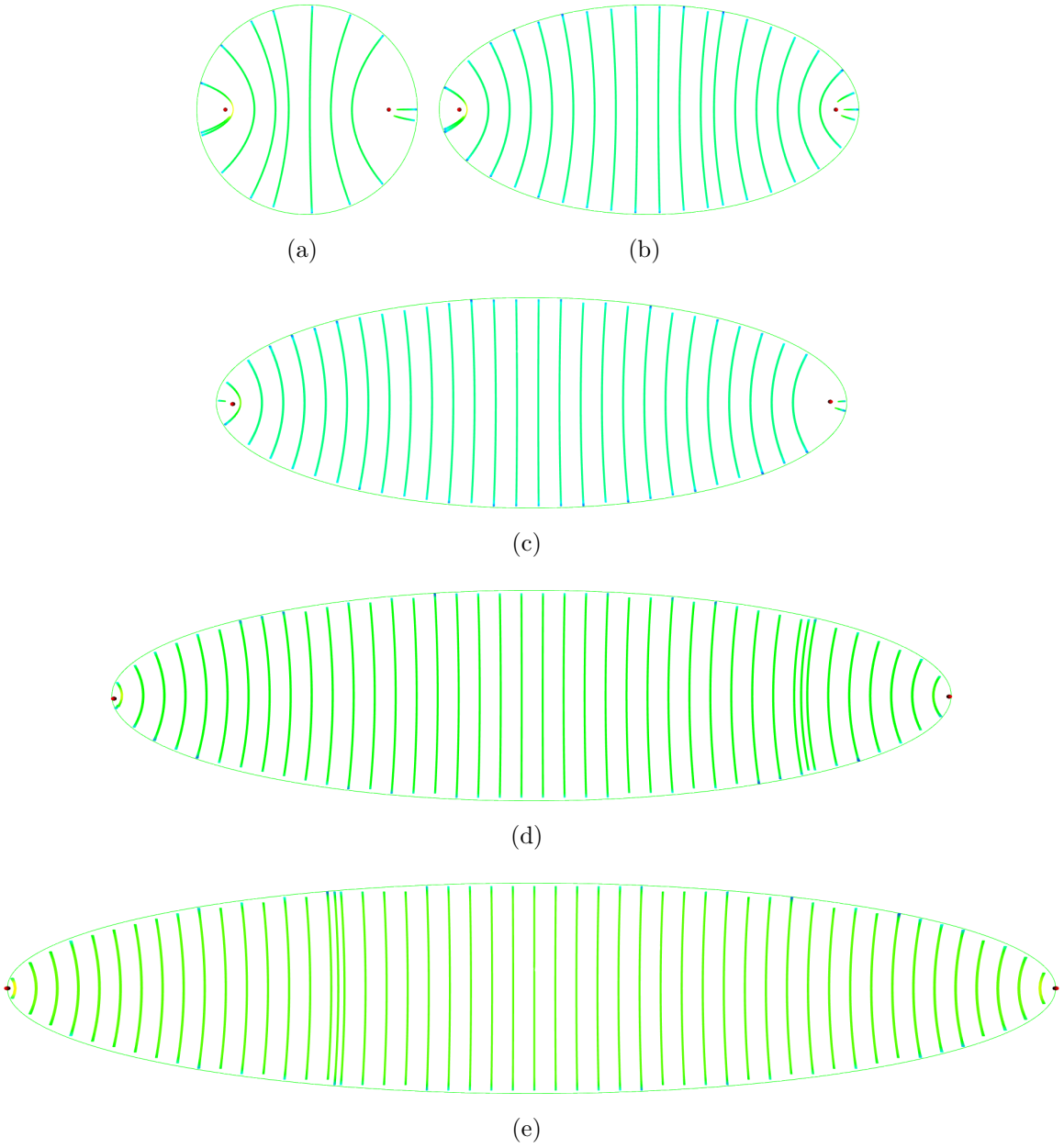

Figure 4.4: Hyperstreamline visualizations of post-driven ground state textures of domains with $a_r = 1 \rightarrow 5$ with strong anchoring and electric field conditions.

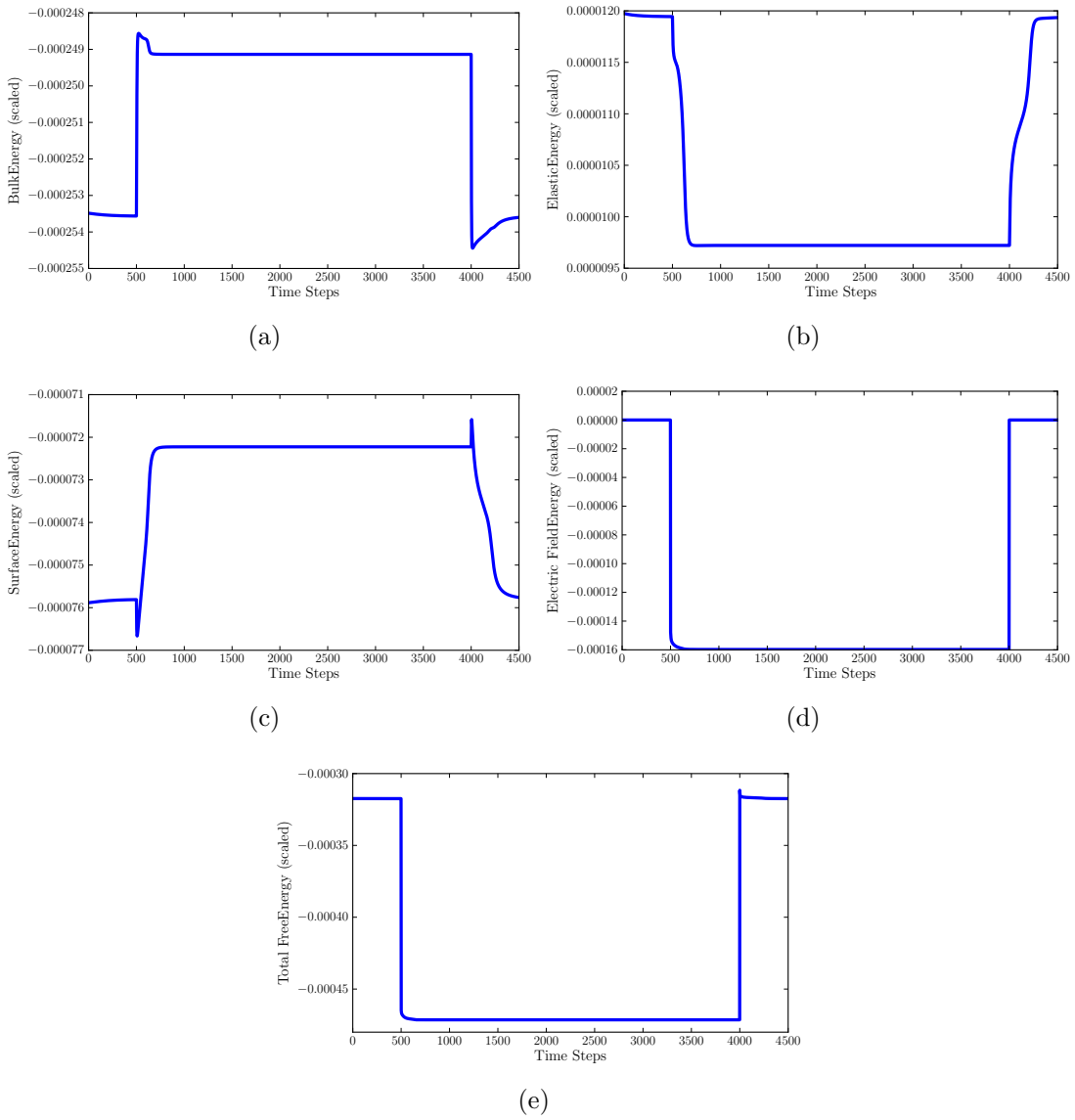

Figure 4.5: Free energy versus time step for the simulation with $a_r = 3$ and the field along the long-axis: (a) bulk free energy, (b) elastic energy, (c) surface energy, (d) electric field energy, and (e) total free energy components.

to the average orientational axis of the steady-state domain (short axis). Thus, the bulk alignment of the domain will initially be weakened by the external field which will induce

bulk reorientation which will require (topologically) translation of disclination defects to the poles along the short axis.

4.3.1 Application of External Field

Figure 4.6 shows the driven state in the presence of the external field for domains with aspect ratios from $a_r = 1 \rightarrow 5$. In all cases, significant reorientation of the domain texture has resulted from the stress contributed by the external field. While bulk alignment conforms well along the field direction, there are significant regions of curvature along the boundaries where the bulk texture and surface anchoring are incommensurate. In contrast to the previous driven texture, the surface anchoring in the focal region is relatively enhanced by the application of the field, as opposed to the regions near the poles of the short-axis which exhibit large distortions with respect to the prefered alignment (normal to the boundary). Another significant observation is that bulk order (S) throughout the domain is diminished which results from the incomptability of the preferred orientation of the field and that of the surface anchoring/geometry. Since the degree of bulk nematic order is proportional to its susceptibility to the electric field (eqn. 4.8), it follows that by reducing the degree of nematic order, the domain reduces its propensity to align with the field.

Figure 4.7 shows the different components of the total free energy of the domain prior to and following application of the external field. Unlike the previous case, there is no distinct short and long timescale dynamics. Only long timescale dynamics are observed that are complex and non-monotonic, which results from defect motion in the domain. While these dynamics are captured in the simulations, they are not addressed in this work due to the complexity of visualization and interpretation of the evolving textures. Although, it is clear in Figures 4.7a-c that application of the field is not commensurate with short-range (S), long-range ($\boldsymbol{n}$), or surface anchoring in that the energies associated with each of these three components increases in the driven state.

4.3.2 Release of External Field

Figure 4.8 shows ground state textures following relaxation of the nematic alignment after cessation of the electric field. Once again, the driven state is no longer stable and thus the domain evolves to new a steady-state. The new steady-state is substantially different from the initial steady-state. The initial steady-state was observed to have an average nematic alignment along the short axis, while all post-field ground states exhibit extremely deformed

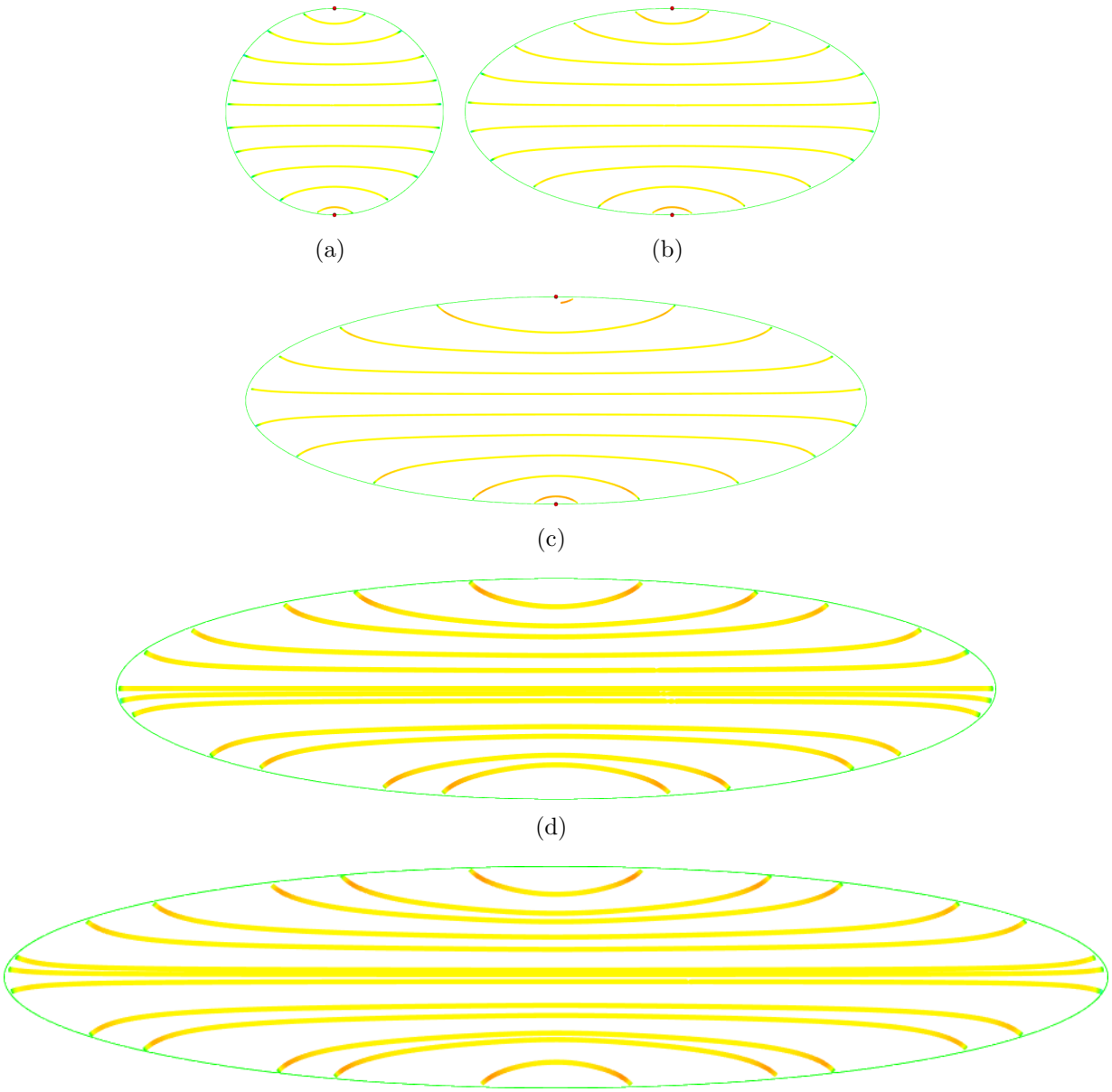

Figure 4.6: Hyperstreamline visualizations of post-driven steady-state textures of domains with $a_r = 1 \rightarrow 5$ with strong anchoring and electric field conditions.

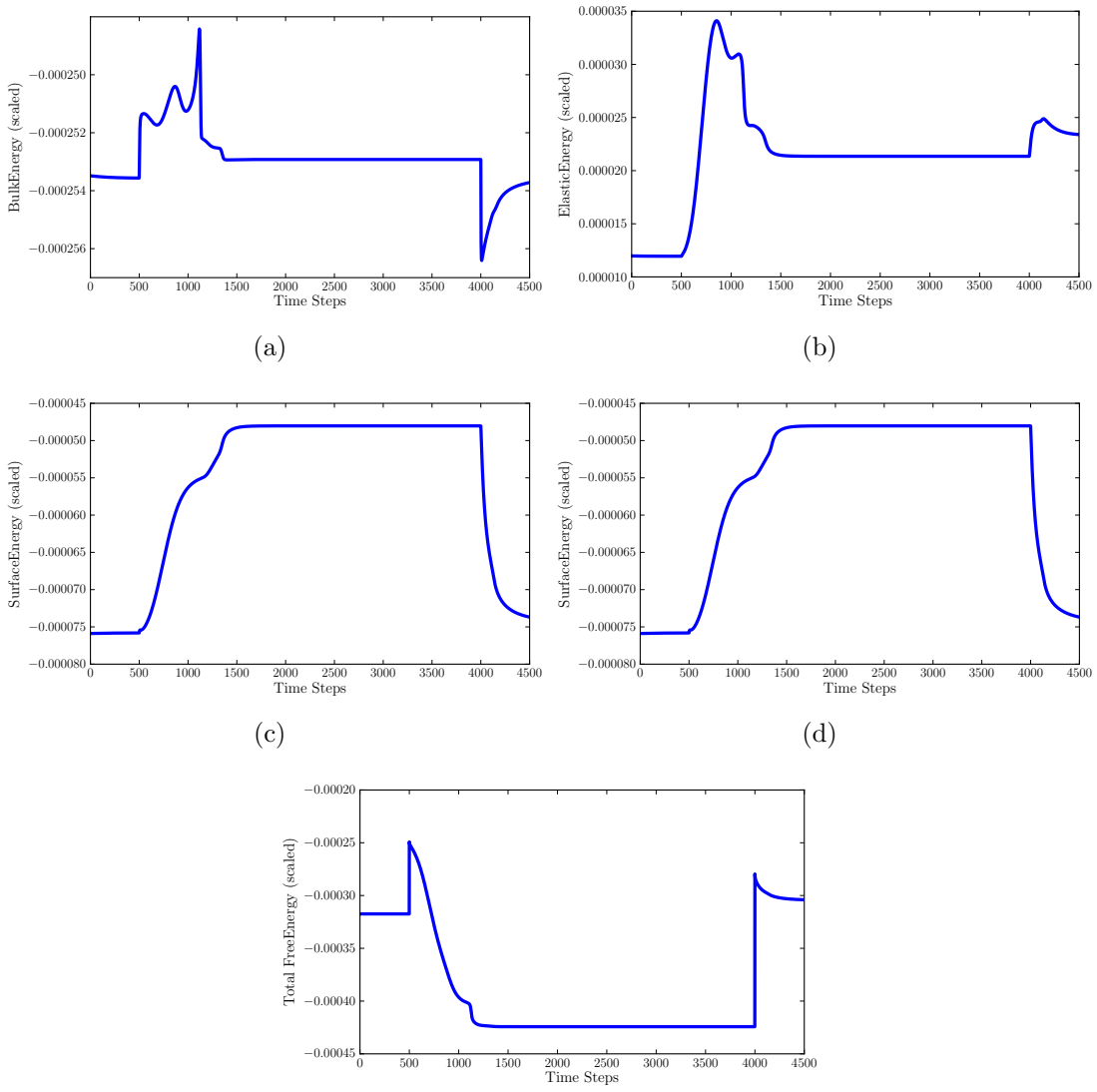

Figure 4.7: Free energy versus timestep for the simulation with $a_r = 3$ and the field along the long-axis: (a) bulk free energy, (b) elastic energy, (c) surface energy, (d) electric field energy, and (e) total free energy components.

textures without a discernible dominant orientational axis. Furthermore, defect locations are far from the high curvature focal regions and instead near regions of low curvature in

the boundary, which suggests that this is a metastable texture. The total free energy for the domain with $a_r = 3$ (Figure 4.7e) supports this observation in that the energy is lower before the field than after. Thus there likely exists a critical field strength below which the texture relaxes to its original state, below the field strength applied in these simulations.

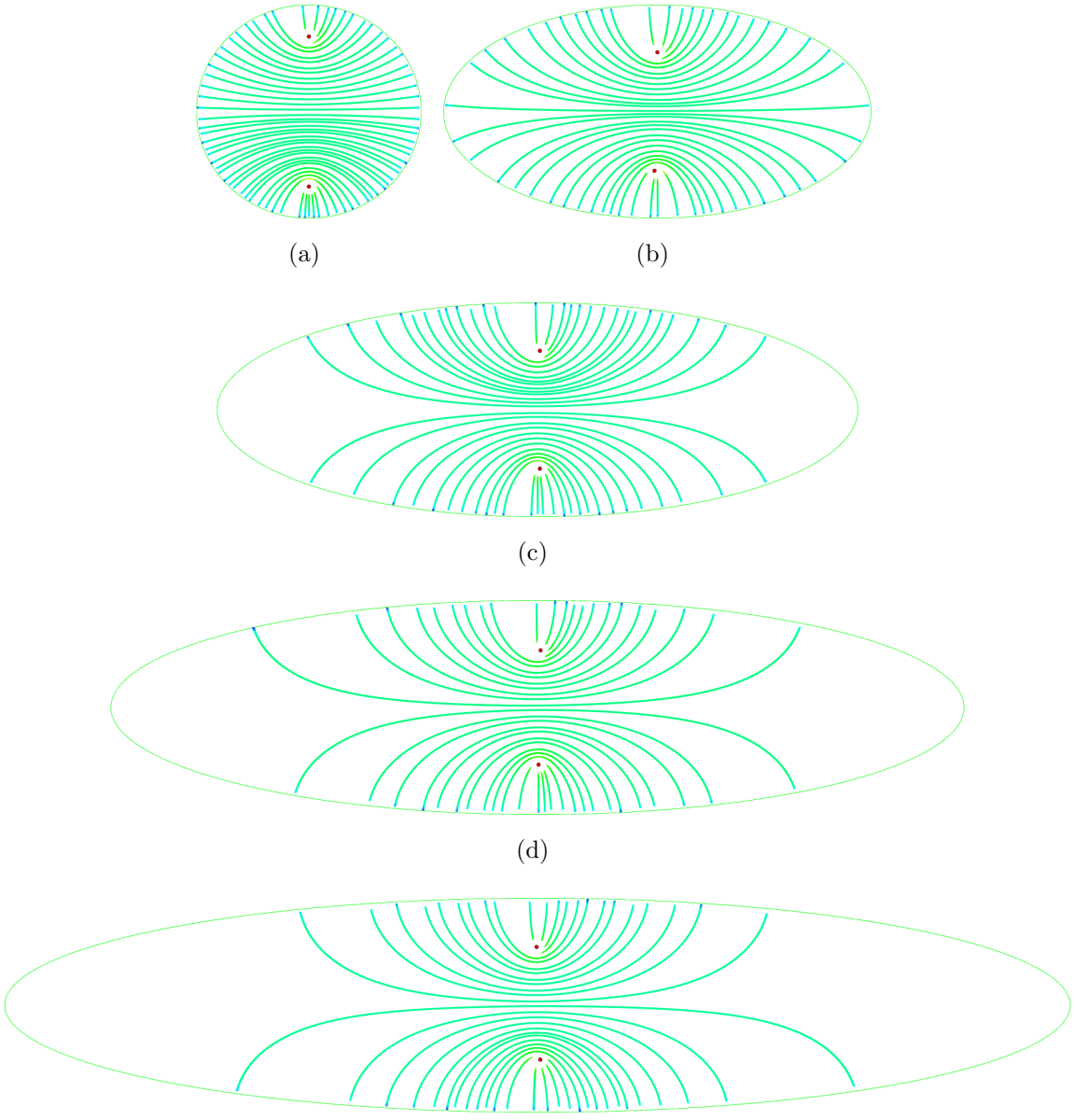

Figure 4.8: Hyperstreamline visualizations of post-driven ground state textures of domains with $a_r = 1 \rightarrow 5$ with strong anchoring and electric field conditions.

Chapter 5

Conclusions

5.1 Conclusions

In this work, a simulation-based study was performed of the formation of the elliptic cylinder nematic domain, the resulting domain texture in the presence of an external field, and the domain texture following release of the external field. The effects of geometry (aspect ratio), surface anchoring, and external field strength were analyzed and found to have a complex interdependence on the character of the nematic reorientation dynamics. The general conclusions of this work are:

1. Formation and reorientation dynamics are complex and governed by the motion of nematic defects through the domain.

2. Surface anchoring conditions may enable "escape" of nematic defects which results in different modes of reorientation dynamics.

3. Geometry of the domain, specifically aspect ratio, strongly affects domain texture by providing regions of high curvature which attract nematic defects.

4. This work supports the application of this computational approach for optimal design of liquid crystal domains based upon requirements for nematic texture and switching dynamics.

5.2 Recommendations

1. Many simplifications were made in this study with respect to the target nematic domain – a spheroid as is present in nematic PDLC films. It is recommended that future studies remove this simplifications in the following order:

   (a) *Three-dimensional domains* – full three-dimensional domains should simulated which will capture additional phenomena such as boundary and defect curvature.

   (b) *Thermal Fluctuations* – a full Langevin dynamics formulation should be used to take into account thermal fluctuations which could destabilize meta-stable textures and avoid issues with saddle point domains.

   (c) *Hydrodynamics* – the coupling between reorientation dynamics and flow is not negligible for "strong" external field strengths, a full hydrodynamic formulation should be used to capture this.

2. The parameters varied in this study included aspect ratio, surface anchoring strength, and field strength – it is recommended that future studies limit this parameter to those of technological significance as opposed to those accessible in an experimental environment.

3. While not analyzed in this work, observed reorientation dynamics are complex and should be evaluated in the future using a set of characteristics that relate to the desired optical properties of the domain:

   (a) *average domain orientation* (vector) – the weighted average of the long-range order of the domain ($\boldsymbol{n}$).

   (b) *domain orientational order parameter* (scalar) – the degree to which the domain orientation conforms to the average domain orientation.

   (c) *driven-state timescale* (scalar) – the timescale within which the domain transitions from the ground state to the driven state.

   (d) *relaxation timescale* (scalar) – the timescale within which the domain transitions from the driven state to the ground state.

APPENDICES

S Calculations

Average of $\cos^2\theta$:

$$f(\theta) = \frac{1}{\text{Surface Area}} \qquad , \qquad \text{Surface Area} = \int_0^{\phi}\int_0^{\theta_u} \sin\theta d\theta d\phi = \phi(1-\cos\theta_u)$$

$$\phi = 2\pi \Longrightarrow \text{Surface Area} = 2\pi(1-\cos\theta_u) \qquad , \qquad f(\theta) = \frac{1}{2\pi(1-\cos\theta_u)}$$

$$< \cos^2\theta >= \iint f(\theta)\cos^2\theta\sin\theta d\theta d\phi = \frac{1}{2\pi(1-\cos\theta_u)}\int_0^{2\pi} d\phi \int_0^{\theta_u} \cos^2\theta\sin\theta d\theta$$

$$= \frac{2\pi}{2\pi(1-\cos\theta_u)}[\frac{-\cos^3\theta}{3}]_0^{\theta_u} \qquad , \qquad \theta_u = \pi \Longrightarrow < cos^2\theta >= \frac{1}{3}$$

Calculation of S when all of molecules are in one direction:

$$S = \iint \frac{1}{2\pi(1-\cos\theta_u)}\frac{1}{2}(3\cos^2\theta - 1)\sin\theta d\theta d\phi$$

$$S = \frac{1}{4\pi(1-\cos\theta_u)}\int_0^{2\pi} d\phi \int_0^{\theta_u} (3\cos^2\theta\sin\theta - \sin\theta)d\theta = \frac{-\cos^3\theta_u + \cos\theta_u}{2(1-\cos\theta_u)}$$

$$S = \lim_{\theta_u \to 0} \frac{-\cos^3\theta_u + \cos\theta_u}{2(1-\cos\theta_u)}$$

$$\lim_{\theta_u \to 0} \cos\theta_u = 1 - \frac{\theta_u^2}{2!} + \frac{\theta_u^4}{4!} - \frac{\theta_u^6}{6!} + \cdots$$

$$S = \lim_{\theta_u \to 0} \frac{-(1-\frac{\theta_u^2}{2!})^3 + 1 - \frac{\theta_u^2}{2!}}{2(1-1+\frac{\theta_u^2}{2!})} = \lim_{\theta_u \to 0} \frac{\theta_u^2}{\theta_u^2} = 1$$

Q Tensor Decomposition

n and m and l are eigen vectors of Q :

$$Q = S\left(nn - \frac{1}{3}I\right) + P\left(mm - ll\right)$$

$$n \cdot n = 1 \quad m \cdot m = 1 \quad l \cdot l = 1 \quad m \cdot n = 0 \quad l \cdot n = 0 \quad m \cdot l = 0 \quad I \cdot n = n$$

$$Q \cdot n = S\left(nn - \frac{1}{3}I\right) \cdot n + P\left(mm - ll\right) \cdot n$$

$$Q \cdot n = S\left(n(n \cdot n) - \frac{1}{3}(I \cdot n)\right) + P\left(m(m \cdot n) - l(l \cdot n)\right) = S\left(n - \frac{1}{3}n\right) + 0 = \underbrace{\frac{2}{3}S}_{\text{eigenvalue}} \quad n$$

$$Q \cdot m = S\left(nn - \frac{1}{3}I\right) \cdot m + P\left(mm - ll\right) \cdot m$$

$$Q \cdot m = S\left(n(n \cdot m) - \frac{1}{3}(I \cdot m)\right) + P\left(m(m \cdot m) - l(l \cdot m)\right) = S\left(0 - \frac{1}{3}m\right) + P(m - 0)$$

$$Q \cdot m = \underbrace{\left(P - \frac{1}{3}S\right)}_{\text{eigenvalue}} m$$

$$Q \cdot l = S\left(nn - \frac{1}{3}I\right) \cdot l + P\left(mm - ll\right) \cdot l$$

$$Q \cdot l = S\left(n(n \cdot l) - \frac{1}{3}(I \cdot l)\right) + P\left(m(m \cdot l) - l(l \cdot l)\right) = S\left(0 - \frac{1}{3}\right) + P(0 - l)$$

$$Q \cdot l = \underbrace{\left(-P - \frac{1}{3}S\right)}_{\text{eigenvalue}} l$$

Uniform Domain

$$f = \frac{1}{2}a(Q:Q) - \frac{1}{3}b(Q \cdot Q) : Q + \frac{1}{4}(Q:Q)^2 + f_0$$

$$Q:Q = Q_{ij}Q_{ji} \qquad Q_{ij} = S(n_i n_j - \frac{1}{3}\delta_{ij})$$

$$Q_{ij}Q_{ji} = S^2(n_i n_j - \frac{1}{3}\delta_{ij})^2 = S^2(n_i^2 n_j^2 - \frac{2}{3}\delta_{ij} + \frac{\delta_{ij}^2}{9})$$

$$Q_{ij}Q_{ji} = S^2\left(n_i^2(n_j^2) - \frac{2}{3}n_i^2 + \frac{3}{9}\right) = S^2\left(n_i^2 - \frac{2}{3} + \frac{3}{9}\right) = \frac{2}{3}S^2$$

$$(Q \cdot Q) : Q = (Q_{ik}Q_{kj})\,Q = S^2\left(n_i n_k - \frac{1}{3}\delta_{ik}\right)\left(n_k n_j - \frac{1}{3}\delta_{kj}\right)Q_{ji}$$

$$(Q \cdot Q) : Q = S^2\left(n_i n_j n_k^2 - \frac{1}{3}n_i n_k \delta_{kj} - \frac{1}{3}n_k n_j \delta_{ik} + \frac{1}{9}\delta_{ik}\delta_{kj}\right)Q_{ji}$$

$$(Q \cdot Q) : Q = S^2\left(n_i n_j - \frac{1}{3}n_i n_j - \frac{1}{3}n_i n_j + \frac{1}{9}\delta_{ij}\right)Q_{ji}$$

$$(Q \cdot Q) : Q = S^3 \left(\frac{1}{3} n_i^2 n_j^2 - \frac{1}{9} n_i n_j \delta_{ji} + \frac{1}{9} n_j n_i \delta_{ij} - \frac{1}{27} \delta_{ij} \delta_{ji} \right) = \frac{2}{3} S^3$$

$$(Q : Q)^2 = \left(\frac{2}{3} S^2 \right)^2 = \frac{4}{9} S^4$$

$$\implies \qquad f = \frac{1}{3} a S^2 - \frac{2}{27} b S^3 + \frac{1}{9} c S^4 + f_0$$

$$\implies \qquad \underbrace{\frac{df}{ds} = \frac{2}{3} a S - \frac{2}{9} b S^2 + \frac{4}{9} c S^3 = 0}_{\text{at equilibrium}}$$

Euler Equation For Tensorial Free Energy:

Euler Equation For Tensorial Free Energy:

$$F[Q] = \iiint_V f(Q_{ij}, Q_{ij,k})\, dV \quad + \quad \iint_A \gamma(Q_{ij})\, dA$$

Q_{ij} and $Q_{ij,k}$ are functions of $x_m \quad m = 1, 2, 3$

$$Q_{ij,k} = \frac{\partial Q_{ij}}{\partial x_k}$$

$$Q_{ij} = \widetilde{Q}_{ij} + \alpha v_{ij} \quad \implies \quad Q_{ij,k} = \widetilde{Q}_{ij,k} + \alpha v_{ij,k}$$

$$F[Q] = \iiint_V f(\widetilde{Q}_{ij} + \alpha v_{ij}, \widetilde{Q}_{ij,k} + \alpha v_{ij,k})\, dV \quad + \quad \iint_A \gamma(\widetilde{Q}_{ij} + \alpha v_{ij})\, dA$$

$\implies F$ is a function of $\alpha_{ij} \implies \nabla F = 0$ at extremum

$$\frac{\partial F}{\partial \alpha_{ij}} = \iiint_V \left[\frac{\partial f}{\partial Q_{ij}} \frac{\partial Q_{ij}}{\partial \alpha_{ij}} + \sum_k \frac{\partial f}{\partial \alpha_{ij,k}} \frac{\partial Q_{ij,k}}{\partial \alpha_{ij}} \right] dV \quad + \quad \iint_A \frac{\partial \gamma}{\partial Q_{ij}} \frac{\partial Q_{ij}}{\partial \alpha_{ij}} \, dA$$

$$\frac{\partial}{\partial x_k} \left(\frac{\partial f}{\partial Q_{ij,k}} v_{ij} \right) \left[\frac{\partial f}{\partial Q_{ij}} v_{ij} + \sum_k \frac{\partial f}{\partial Q_{ij,k}} v_{ij,k} \right] dV \quad + \quad \iint_A \frac{\partial \gamma}{\partial Q_{ij}} v_{ij} \, dA$$

$$\sum_k \frac{\partial f}{\partial Q_{ij,k}} v_{ij,k} = \sum_k \left(\frac{\partial}{\partial x_k} \left(\frac{\partial f}{\partial Q_{ij,k}} v_{ij} \right) - \frac{\partial}{\partial x_k} \left(\frac{\partial f}{\partial Q_{ij,k}} \right) v_{ij} \right)$$

$$\frac{\partial F}{\partial \alpha_{ij}} = \iiint_V \left[\frac{\partial f}{\partial Q_{ij}} v_{ij} + \sum_k \left(\frac{\partial}{\partial x_k} \left(\frac{\partial f}{\partial Q_{ij,k}} v_{ij} \right) - \frac{\partial}{\partial x_k} \left(\frac{\partial f}{\partial Q_{ij,k}} \right) v_{ij} \right) \right] dV \quad +$$

$$\iint_A \frac{\partial \gamma}{\partial Q_{ij}} v_{ij} \, dA$$

Divergence Theorem:

$$\iiint_V \nabla . \left(\frac{\partial}{\partial x_1} \left(\frac{\partial f}{\partial Q_{ij,1}} \right) v_{ij}, \frac{\partial}{\partial x_2} \left(\frac{\partial f}{\partial Q_{ij,2}} \right) v_{ij}, \frac{\partial}{\partial x_3} \left(\frac{\partial f}{\partial Q_{ij,3}} \right) v_{ij} \right) dV =$$

$$\iint_A \left[\frac{\partial f}{\partial Q_{ij,1}} n_1 + \frac{\partial f}{\partial Q_{ij,2}} n_2 + \frac{\partial f}{\partial Q_{ij,3}} n_3 \right] v_{ij} \, dA$$

$$n = (n_1, n_2, n_3) \quad \text{Unit Normal Vector}$$

$$\implies \frac{\partial F}{\partial \alpha_{ij}} = \iiint_V \left[\frac{\partial f}{\partial Q_{ij}} - \sum_k \frac{\partial}{\partial x_k} \left(\frac{\partial f}{\partial Q_{ij,k}} \right) \right] v_{ij} \, dV \quad +$$

$$\iint_A \left[\frac{\partial \gamma}{\partial Q_{ij}} + \sum_k \frac{\partial f}{\partial Q_{ij,k}} n_k \right] dA$$

$$\frac{\partial F}{\partial \alpha_{ij}} = 0 \quad \Longrightarrow \quad \frac{\partial f}{\partial Q_{ij}} - \sum_k \frac{\partial}{\partial x_k} \left(\frac{\partial f}{\partial Q_{ij,k}} \right) = 0 \quad i,j = 1,2,3$$

$$\underbrace{\frac{\partial f}{\partial Q} - \nabla . \left(\frac{\partial f}{\partial \left(\nabla Q \right)} \right) = 0}_{\text{Euler–Lagrange Equation}}$$

$$\frac{\partial \gamma}{\partial Q_{ij}} + \sum_k \frac{\partial f}{\partial Q_{ij,k}} n_k = 0 \quad \Longrightarrow \quad \underbrace{\frac{\partial \gamma}{\partial Q} + \frac{\partial f}{\partial \left(\nabla Q \right)} \cdot \vec{n} = 0}_{\text{Boundary Condition}}$$

Dynamics Equation

$$\mu \frac{\partial Q}{\partial t} = - \left(\frac{\partial f}{\partial Q} - \nabla . \left(\frac{\partial f}{\partial \left(\nabla Q \right)} \right) \right)$$

$$f = \frac{1}{2} a (Q:Q) - \frac{1}{3} b (Q \cdot Q) : Q + \frac{1}{4} c (Q:Q)^2 + \frac{1}{2} l_1 \left((\nabla Q)^T \vdots (\nabla Q)^T \right) -$$

$$- \frac{\varepsilon_\circ}{8\pi} \left[\left(\frac{\varepsilon_\parallel + 2\varepsilon_\perp}{3} I + (\varepsilon_\parallel - \varepsilon_\perp) Q \right) \right] : EE$$

$$\frac{\partial f}{\partial Q_{ij}} = \frac{1}{2}a\frac{\partial}{\partial Q_{ij}}\left(\sum_k\sum_l Q_{kl}Q_{lk}\right) - \frac{1}{3}b\frac{\partial}{\partial Q_{ij}}\left(\sum_k\sum_l\sum_m Q_{kl}Q_{lm}Q_{mk}\right) +$$

$$\frac{1}{4}c\frac{\partial}{\partial Q_{ij}}\left(\left(\sum_k\sum_l Q_{kl}Q_{lk}\right)^2\right) - \frac{\varepsilon_\circ}{8\pi}(\varepsilon_\parallel - \varepsilon_\perp)\frac{\partial}{\partial Q_{ij}}\left(\sum_k\sum_l Q_{kl}E_lE_k\right)$$

Derivative is a linear operator $\Longrightarrow$

$$\frac{\partial f}{\partial Q_{ij}} = \frac{1}{2}a\sum_k\sum_l\frac{\partial}{\partial Q_{ij}}\left(Q_{kl}Q_{lk}\right) - \frac{1}{3}b\sum_k\sum_l\sum_m\frac{\partial}{\partial Q_{ij}}\left(Q_{kl}Q_{lm}Q_{mk}\right) +$$

$$\frac{1}{4}c\sum_k\sum_l\sum_m\sum_n\frac{\partial}{\partial Q_{ij}}\left(Q_{kl}Q_{lk}Q_{mn}Q_{nm}\right) - \frac{\varepsilon_\circ}{8\pi}(\varepsilon_\parallel - \varepsilon_\perp)\sum_k\sum_l\frac{\partial}{\partial Q_{ij}}(Q_{kl}E_lE_k)$$

$$\frac{\partial f}{\partial Q_{ij}} = \frac{1}{2}a(Q_{ij}+Q_{ji}) - \frac{1}{3}b\left(\sum_m Q_{jm}Q_{mi} + \sum_k Q_{ki}Q_{jk} + \sum_l Q_{jl}Q_{li}\right) +$$

$$\frac{1}{4}c\left(\sum_m\sum_n Q_{ji}Q_{mn}Q_{nm} + \sum_m\sum_n Q_{ji}Q_{mn}Q_{nm} + \sum_k\sum_l Q_{ji}Q_{kl}Q_{lk} + \sum_k\sum_l Q_{ji}Q_{kl}Q_{lk}\right) -$$

$$\frac{\varepsilon_\circ}{8\pi}(\varepsilon_\parallel - \varepsilon_\perp)(E_iE_j)$$

$$\frac{\partial f}{\partial Q} = aQ - b(Q\cdot Q) + c(Q:Q)Q - \frac{\varepsilon_\circ}{8\pi}(\varepsilon_\parallel - \varepsilon_\perp)EE$$

$$\frac{\partial f}{\partial(\nabla Q)} = \frac{\partial f}{\partial Q_{ij,k}} = \frac{\partial}{\partial Q_{ij,k}}\left(\frac{1}{2}l_1\left((\nabla Q)^T\vdots(\nabla Q)^T\right)\right)$$

$$\frac{\partial f}{\partial Q_{ij,k}} = \frac{1}{2} l_1 \frac{\partial}{\partial Q_{ij,k}} \left(\sum_l \sum_m \sum_n \frac{\partial Q_{ln}}{\partial x_m} \frac{\partial Q_{nl}}{\partial x_m} \right)$$

$$\frac{\partial f}{\partial Q_{ij,k}} = \frac{1}{2} l_1 \sum_l \sum_m \sum_n \frac{\partial}{\partial Q_{ij,k}} (Q_{ln,m} Q_{nl,m})$$

$$\frac{\partial f}{\partial Q_{ij,k}} = \frac{1}{2} l_1 (Q_{ij,k} + Q_{ji,k}) = l_1 Q_{ij,k}$$

$$\nabla \cdot \left(\frac{\partial f}{\partial (\nabla Q)} \right) = \sum_k \frac{\partial}{\partial x_k} \left(\frac{\partial f}{\partial (Q_{ij,k})} \right)$$

$$\nabla \cdot \left(\frac{\partial f}{\partial (\nabla Q)} \right) = l_1 \sum_k \frac{\partial (Q_{ij,k})}{\partial x_k} = l_1 \sum_k Q_{ij,kk}$$

$$\nabla \cdot \left(\frac{\partial f}{\partial (\nabla Q)} \right) = l_1 \nabla^2 Q$$

$$\implies \quad \mu \frac{\partial Q}{\partial t} = - \left(aQ - b(Q \cdot Q) + c(Q : Q)Q - \frac{\varepsilon_\circ}{8\pi} (\varepsilon_\parallel - \varepsilon_\perp) EE - l_1 \nabla^2 Q \right)$$

Dimensionless Euler-Lagrange Equation

$$\frac{\partial Q_{ij}}{\partial \widetilde{t}} = -(\widetilde{T} - 1) Q_{ij} + \frac{b}{a_0 T_{NI}} \sum_k Q_{ik} Q_{kj} - \frac{c}{a_0 T_{NI}} Q_{ij} \sum_m \sum_n Q_{mn} Q_{nm} +$$

$$\frac{\varepsilon_\circ}{8a_0T_{NI}\pi}(\varepsilon_\parallel - \varepsilon_\perp)E_iE_j + \frac{l_1}{a_0T_{NI}l^2}\frac{\partial^2 Q_{ij}}{\partial x^2} - \frac{1}{3a_0T_{NI}}\left(b\sum_k\sum_n Q_{nk}Q_{kn} + \sum_k \frac{\varepsilon_\circ}{8\pi}(\varepsilon_\parallel - \varepsilon_\perp)E_kE_k\right)I_{ij}$$

References

[1] Otto Lehmann. On flowing crystals. *Zeitschrift für Physikalische Chemie*, 4:462, 1889.

[2] S. Chandrasekhar. *Liquid Crystals*. Cambridge University Press, Cambridge, second edition, 1992.

[3] P.G. de Gennes and J Prost. *The Physics of Liquid Crystals*. Oxford University Press, New York, second edition, 1995.

[4] Birendra Bahadur, editor. *Liquid Crystals : Applications and Uses Vol. 3*. World Scientific Publishing Co. Pte. Ltd., 1990.

[5] FC Frank. I. liquid crystals. on the theory of liquid crystals. *Discussions of the Faraday Society*, 25:19–28, 1958.

[6] Denis Andrienko. *Introduction to liquid crystals*. International Max Planck Research School, 2006.

[7] Claes Johnson. *Numerical solution of partial differential equations by the finite element method*. Cambridge University Press, 1987.

[8] Ingo Dierking. *Textures of Liquid Crystals*. Wiley and Sons, 2003.

[9] Jean-Claude Toledano and Pierre Toledano. *The Landau Theory of Phase Transitions: Application to Structural, Incommensurate, Magnetic, and Liquid Crystal Systems (World Scientific Lecture Notes in Physics)*. World Scientific Pub Co Inc, 1987.

[10] P. M. Chaikin and T. C. Lubensky. *Principles of condensed matter physics*. Cambridge Univ Press, 1995.

[11] Peter J. Collings and Michael Hird. *Introduction to liquid crystals chemistry and physics*. Taylor & Francis, 1997.

[12] B. Wincure and A.D. Rey. Interfacial nematodynamics of heterogeneous curved isotropic-nematic moving fronts. *The Journal of Chemical Physics*, 124(24):244902, 2006.

[13] Giovanni Barbero and Luiz Roberto Evangelista. *Adsorption phenomena and anchoring energy in nematic liquid crystals*. CRC Press, 2005.

[14] G. Barbero and Luiz Roberto Evangelista. *An Elementary Course on the Continuum Theory for Nematic Liquid Crystals (Series on Liquid Crystals , Vol 3)*. World Scientific Publishing Company, 2000.

[15] Renata-Maria Marroum, Germano S. Iannacchione, Daniele Finotello, and Michael A. Lee. Numerical study of cylindrically confined nematic liquid crystals. *Physical Review E: Statistical Physics, Plasmas, Fluids, and Related Interdisciplinary Topics*, 51:R2743–R2746, 1995.

[16] A. Sonnet, A. Kilian, and S. Hess. Alignment tensor versus director: Description of defects in nematic liquid crystals. *Phys. Rev. E*, 52(1):718–722, Jul 1995.

[17] A. M. Sonnet and S. Hess. *Defects in liquid crystals: computer simulations, theory & experiments*, chapter Alignment tensor versus director description in nematic liquid crystals, pages 17–33. Springer, 2001.

[18] J. Fukuda and H. Yokoyama. Director configuration and dynamics of a nematic liquid crystal around a two-dimensional spherical particle: Numerical analysis using adaptive grids. *The European Physical Journal E: Soft Matter and Biological Physics*, 4(3):389–396, March 2001.

[19] J. Yan and A. D. Rey. Texture formation in carbonaceous mesophase fibers. *Phys. Rev. E*, 65(3):031713, Feb 2002.

[20] Gino De Luca and Alejandro D. Rey. Ringlike cores of cylindrically confined nematic point defects. *The Journal of Chemical Physics*, 126(9):094907, 2007.

[21] H. J. Coles and C. Strazielle. The order-disorder phase transition in liquid crystals as a function of molecular structure. i. the alkyl cyanobiphenyls. *Mol. Cryst. Liq. Cryst.*, 55:237–50, 1979.

[22] AK Bhattacharjee, Gautam I Menon, and R Adhikari. Fluctuating dynamics of nematic liquid crystals using the stochastic method of lines. *The Journal of chemical physics*, 133:044112, 2010.

[23] M. Kleman and O.D. Lavrentovich. *Soft Matter Physics: An Introduction*. Springer, New York, first edition, 2003.

[24] Rashmi C. Desai and Raymond Kapral. *Dynamics of Self-Organized and Self-Assembled Structures*. Cambridge University Press, 2009.

[25] A. K. Bhattacharjee, Gautam I. Menon, and R. Adhikari. Numerical method of lines for the relaxational dynamics of nematic liquid crystals, 2008.

[26] A. A. Sonin. *The surface physics of liquid crystals*. Gordon and Breach, 1995.

[27] M. Kleman. Defects in liquid crystals. *Reports on Progress in Physics*, 52:555–654, 1989.

[28] Paul S. Drzaic. *Liquid Crystal Dispersions*, volume 1 of *Liquid Crystals Series*. World Scientific, 1995.

[29] P. Drzaic. Putting liquid crystal droplets to work: a short history of polymer dispersed liquid crystals. *Liq. Cryst.*, 33(11):1281–1296, 2006.

[30] Daniel Fleisch. *A Student's guide to Maxwell's equations*. Cambridge University Press, 2008.

[31] William B Krantz. *Scaling analysis in modeling transport and reaction processes: a systematic approach to model building and the art of approximation*. Wiley. com, 2007.

[32] H. J. Coles and C. Strazielle. Pretransitional behavior of the direct isotropic to smectic a phase transition of dodecylcyanobiphenyl (12cb). *Mol. Cryst. Liq. Cryst.*, 49:259–64, 1979.

[33] Tiezheng Qian and Ping Sheng. Generalized hydrodynamic equations for nematic liquid crystals. *Phys. Rev. E*, 58(6):7475–7485, Dec 1998.

[34] J. Fukuda and H. Yokoyama. Stability of the director profile of a nematic liquid crystal around a spherical particle under an external field. *The European Physical Journal E: Soft Matter and Biological Physics*, 21(4):341–347, December 2006.